Investigation of the Decay of Orbitally-Excited B Mesons and First Measurement of the Branching Ratio $\mathrm{BR}(\mathrm{B}_J^* \to \mathrm{B}^*\pi(X))$

The OPAL Collaboration

Abstract

From about 4 million hadronic Z^0 decays recorded by the OPAL detector on and near to the Z^0 resonance, we select a sample of more than $570\,000$ inclusively reconstructed B mesons. Orbitally-excited mesons B_J^* are reconstructed using $\mathrm{B}\pi^{\pm}$ combinations. Independently, B^* mesons are reconstructed using the decay $\mathrm{B}^* \to \mathrm{B}\gamma$. The selected B^* candidates are used to obtain samples enriched or depleted in the decay $\mathrm{B}_J^* \to \mathrm{B}^*\pi^{\pm}(X)$, where (X) refers to decay modes with or without additional accompanying decay particles. From the number of signal candidates in the $\mathrm{B}\pi^{\pm}$ mass spectra of these two samples, we perform the first measurement of the branching ratio of orbitally-excited B mesons decaying into $\mathrm{B}^*\pi(X)$:

$$\mathrm{BR}(\mathrm{B}_J^* \to \mathrm{B}^*\pi(X)) = 0.85\,^{+0.26}_{-0.27} \pm 0.12\,,$$

where the first error is statistical and the second systematic. If B_J^* decay modes other than single pion transitions can be neglected the measured ratio corresponds to the branching ratio $\mathrm{BR}(\mathrm{B}_J^* \to \mathrm{B}^*\pi)$.

In the framework of Heavy Quark Symmetry, a simultaneous fit to the $\mathrm{B}\pi^{\pm}$ mass spectra of the samples enriched or depleted in $\mathrm{B}_J^* \to \mathrm{B}^*\pi^{\pm}(X)$ decays yields the mass and the width of the $\mathrm{B}_1(3/2)$ state, as well as the branching ratio of B_J^* mesons decaying into $\mathrm{B}^*\pi$:

$$
\begin{aligned}
M(\mathrm{B}_1(3/2)) &= (\, 5.738\,^{+\,0.005}_{-\,0.006} \pm 0.007\,)\,\mathrm{GeV}/c^2 \\
\Gamma(\mathrm{B}_1(3/2)) &= (\, 18\,^{+\,15\,+\,29}_{-\,13\,-\,23}\,)\,\mathrm{MeV}/c^2 \\
\mathrm{BR}(\mathrm{B}_J^* \to \mathrm{B}^*\pi) &= 0.74\,^{+\,0.12\,+\,0.21}_{-\,0.10\,-\,0.15}\,,
\end{aligned}
$$

where the uncertainties are statistical and systematic, respectively.

arXiv:hep-ex/0010031v1 13 Oct 2000

The OPAL Collaboration

G. Abbiendi[2], K. Ackerstaff[8], C. Ainsley[5], P.F. Åkesson[3], G. Alexander[22], J. Allison[16],
K.J. Anderson[9], S. Arcelli[17], S. Asai[23], S.F. Ashby[1], D. Axen[27], G. Azuelos[18,a], I. Bailey[26],
A.H. Ball[8], E. Barberio[8], R.J. Barlow[16], S. Baumann[3], T. Behnke[25], K.W. Bell[20], G. Bella[22],
A. Bellerive[9], G. Benelli[2], S. Bentvelsen[8], S. Bethke[32], O. Biebel[32], I.J. Bloodworth[1],
O. Boeriu[10], P. Bock[11], J. Böhme[14,h], D. Bonacorsi[2], M. Boutemeur[31], S. Braibant[8],
P. Bright-Thomas[1], L. Brigliadori[2], R.M. Brown[20], H.J. Burckhart[8], J. Cammin[3], P. Capiluppi[2],
R.K. Carnegie[6], A.A. Carter[13], J.R. Carter[5], C.Y. Chang[17], D.G. Charlton[1,b], P.E.L. Clarke[15],
E. Clay[15], I. Cohen[22], O.C. Cooke[8], J. Couchman[15], C. Couyoumtzelis[13], R.L. Coxe[9],
A. Csilling[15,j], M. Cuffiani[2], S. Dado[21], G.M. Dallavalle[2], S. Dallison[16], A. de Roeck[8], E. de
Wolf[8], P. Dervan[15], K. Desch[25], B. Dienes[30,h], M.S. Dixit[7], M. Donkers[6], J. Dubbert[31],
E. Duchovni[24], G. Duckeck[31], I.P. Duerdoth[16], P.G. Estabrooks[6], E. Etzion[22], F. Fabbri[2],
M. Fanti[2], L. Feld[10], P. Ferrari[12], F. Fiedler[8], I. Fleck[10], M. Ford[5], A. Frey[8], A. Fürtjes[8],
D.I. Futyan[16], P. Gagnon[12], J.W. Gary[4], G. Gaycken[25], C. Geich-Gimbel[3], G. Giacomelli[2],
P. Giacomelli[8], D. Glenzinski[9], J. Goldberg[21], C. Grandi[2], K. Graham[26], E. Gross[24],
J. Grunhaus[22], M. Gruwé[25], P.O. Günther[3], C. Hajdu[29], G.G. Hanson[12], M. Hansroul[8],
M. Hapke[13], K. Harder[25], A. Harel[21], M. Harin-Dirac[4], A. Hauke[3], M. Hauschild[8],
C.M. Hawkes[1], R. Hawkings[8], R.J. Hemingway[6], C. Hensel[25], G. Herten[10], R.D. Heuer[25],
J.C. Hill[5], A. Hocker[9], K. Hoffman[8], R.J. Homer[1], A.K. Honma[8], D. Horváth[29,c],
K.R. Hossain[28], R. Howard[27], P. Hüntemeyer[25], P. Igo-Kemenes[11], K. Ishii[23], F.R. Jacob[20],
A. Jawahery[17], H. Jeremie[18], C.R. Jones[5], P. Jovanovic[1], T.R. Junk[6], N. Kanaya[23],
J. Kanzaki[23], G. Karapetian[18], D. Karlen[6], V. Kartvelishvili[16], K. Kawagoe[23], T. Kawamoto[23],
R.K. Keeler[26], R.G. Kellogg[17], B.W. Kennedy[20], D.H. Kim[19], K. Klein[11], A. Klier[24], S. Kluth[32],
T. Kobayashi[23], M. Kobel[3], T.P. Kokott[3], S. Komamiya[23], R.V. Kowalewski[26], T. Kress[4],
P. Krieger[6], J. von Krogh[11], T. Kuhl[3], M. Kupper[24], P. Kyberd[13], G.D. Lafferty[16],
H. Landsman[21], D. Lanske[14], I. Lawson[26], J.G. Layter[4], A. Leins[31], D. Lellouch[24], J. Letts[12],
L. Levinson[24], R. Liebisch[11], J. Lillich[10], B. List[8], C. Littlewood[5], A.W. Lloyd[1], S.L. Lloyd[13],
F.K. Loebinger[16], G.D. Long[26], M.J. Losty[7], J. Lu[27], J. Ludwig[10], A. Macchiolo[18],
A. Macpherson[28,m], W. Mader[3], S. Marcellini[2], T.E. Marchant[16], A.J. Martin[13], J.P. Martin[18],
G. Martinez[17], T. Mashimo[23], P. Mättig[24], W.J. McDonald[28], J. McKenna[27], T.J. McMahon[1],
R.A. McPherson[26], F. Meijers[8], P. Mendez-Lorenzo[31], W. Menges[25], F.S. Merritt[9], H. Mes[7],
A. Michelini[2], S. Mihara[23], G. Mikenberg[24], D.J. Miller[15], W. Mohr[10], A. Montanari[2], T. Mori[23],
K. Nagai[8], I. Nakamura[23], H.A. Neal[12,f], R. Nisius[8], S.W. O'Neale[1], F.G. Oakham[7], F. Odorici[2],
H.O. Ogren[12], A. Oh[8], A. Okpara[11], M.J. Oreglia[9], S. Orito[23], G. Pásztor[8,j], J.R. Pater[16],
G.N. Patrick[20], J. Patt[10], P. Pfeifenschneider[14,i], J.E. Pilcher[9], J. Pinfold[28], D.E. Plane[8],
B. Poli[2], J. Polok[8], O. Pooth[8], M. Przybycień[8,d], A. Quadt[8], C. Rembser[8], P. Renkel[24], H. Rick[4],
N. Rodning[28], J.M. Roney[26], S. Rosati[3], K. Roscoe[16], A.M. Rossi[2], Y. Rozen[21], K. Runge[10],
O. Runolfsson[8], D.R. Rust[12], K. Sachs[6], T. Saeki[23], O. Sahr[31], E.K.G. Sarkisyan[22], C. Sbarra[26],
A.D. Schaile[31], O. Schaile[31], P. Scharff-Hansen[8], M. Schröder[8], M. Schumacher[25], C. Schwick[8],
W.G. Scott[20], R. Seuster[14,h], T.G. Shears[8,k], B.C. Shen[4], C.H. Shepherd-Themistocleous[5],
P. Sherwood[15], G.P. Siroli[2], A. Skuja[17], A.M. Smith[8], G.A. Snow[17], R. Sobie[26],
S. Söldner-Rembold[10,e], S. Spagnolo[20], M. Sproston[20], A. Stahl[3], K. Stephens[16], K. Stoll[10],
D. Strom[19], R. Ströhmer[31], L. Stumpf[26], B. Surrow[8], S.D. Talbot[1], S. Tarem[21], R.J. Taylor[15],
R. Teuscher[9], M. Thiergen[10], J. Thomas[15], M.A. Thomson[8], E. Torrence[9], S. Towers[6],
D. Toya[23], T. Trefzger[31], I. Trigger[8], Z. Trócsányi[30,g], E. Tsur[22], M.F. Turner-Watson[1],

I. Ueda[23], B. Vachon[26], P. Vannerem[10], M. Verzocchi[8], H. Voss[8], J. Vossebeld[8], D. Waller[6], C.P. Ward[5], D.R. Ward[5], P.M. Watkins[1], A.T. Watson[1], N.K. Watson[1], P.S. Wells[8], T. Wengler[8], N. Wermes[3], D. Wetterling[11] J.S. White[6], G.W. Wilson[16], J.A. Wilson[1], T.R. Wyatt[16], S. Yamashita[23], V. Zacek[18], D. Zer-Zion[8,l]

[1]School of Physics and Astronomy, University of Birmingham, Birmingham B15 2TT, UK
[2]Dipartimento di Fisica dell' Università di Bologna and INFN, I-40126 Bologna, Italy
[3]Physikalisches Institut, Universität Bonn, D-53115 Bonn, Germany
[4]Department of Physics, University of California, Riverside CA 92521, USA
[5]Cavendish Laboratory, Cambridge CB3 0HE, UK
[6]Ottawa-Carleton Institute for Physics, Department of Physics, Carleton University, Ottawa, Ontario K1S 5B6, Canada
[7]Centre for Research in Particle Physics, Carleton University, Ottawa, Ontario K1S 5B6, Canada
[8]CERN, European Organisation for Nuclear Research, CH-1211 Geneva 23, Switzerland
[9]Enrico Fermi Institute and Department of Physics, University of Chicago, Chicago IL 60637, USA
[10]Fakultät für Physik, Albert Ludwigs Universität, D-79104 Freiburg, Germany
[11]Physikalisches Institut, Universität Heidelberg, D-69120 Heidelberg, Germany
[12]Indiana University, Department of Physics, Swain Hall West 117, Bloomington IN 47405, USA
[13]Queen Mary and Westfield College, University of London, London E1 4NS, UK
[14]Technische Hochschule Aachen, III Physikalisches Institut, Sommerfeldstrasse 26-28, D-52056 Aachen, Germany
[15]University College London, London WC1E 6BT, UK
[16]Department of Physics, Schuster Laboratory, The University, Manchester M13 9PL, UK
[17]Department of Physics, University of Maryland, College Park, MD 20742, USA
[18]Laboratoire de Physique Nucléaire, Université de Montréal, Montréal, Quebec H3C 3J7, Canada
[19]University of Oregon, Department of Physics, Eugene OR 97403, USA
[20]CLRC Rutherford Appleton Laboratory, Chilton, Didcot, Oxfordshire OX11 0QX, UK
[21]Department of Physics, Technion-Israel Institute of Technology, Haifa 32000, Israel
[22]Department of Physics and Astronomy, Tel Aviv University, Tel Aviv 69978, Israel
[23]International Centre for Elementary Particle Physics and Department of Physics, University of Tokyo, Tokyo 113-0033, and Kobe University, Kobe 657-8501, Japan
[24]Particle Physics Department, Weizmann Institute of Science, Rehovot 76100, Israel
[25]Universität Hamburg/DESY, II Institut für Experimental Physik, Notkestrasse 85, D-22607 Hamburg, Germany
[26]University of Victoria, Department of Physics, P O Box 3055, Victoria BC V8W 3P6, Canada
[27]University of British Columbia, Department of Physics, Vancouver BC V6T 1Z1, Canada
[28]University of Alberta, Department of Physics, Edmonton AB T6G 2J1, Canada
[29]Research Institute for Particle and Nuclear Physics, H-1525 Budapest, P O Box 49, Hungary
[30]Institute of Nuclear Research, H-4001 Debrecen, P O Box 51, Hungary
[31]Ludwigs-Maximilians-Universität München, Sektion Physik, Am Coulombwall 1, D-85748 Garching, Germany
[32]Max-Planck-Institute für Physik, Föhring Ring 6, 80805 München, Germany

[a] and at TRIUMF, Vancouver, Canada V6T 2A3

[b] and Royal Society University Research Fellow

[c] and Institute of Nuclear Research, Debrecen, Hungary

[d] and University of Mining and Metallurgy, Cracow

[e] and Heisenberg Fellow

[f] now at Yale University, Dept of Physics, New Haven, USA

[g] and Department of Experimental Physics, Lajos Kossuth University, Debrecen, Hungary

[h] and MPI München

[i] now at MPI für Physik, 80805 München

[j] and Research Institute for Particle and Nuclear Physics, Budapest, Hungary

[k] now at University of Liverpool, Dept of Physics, Liverpool L69 3BX, UK

[l] and University of California, Riverside, High Energy Physics Group, CA 92521, USA

[m] and CERN, EP Div, 1211 Geneva 23.

1 Introduction

An important prediction of Heavy Quark Effective Theory (HQET) is the existence of an approximate spin-flavour symmetry for hadrons containing one heavy quark Q ($m_Q \gg \Lambda_{\mathrm{QCD}}$) [1]. In the limit $m_Q \to \infty$, mesons composed of a heavy quark Q and a light quark q are characterised by the spin of the heavy quark, S_Q, the total angular momentum of the light quark, $j_q = S_q + L$, and the total angular momentum, J, where S_q and L denote spin and orbital angular momentum of the light quark, respectively. In the heavy quark limit, both S_Q and j_q are good quantum numbers and the total angular momentum of the meson is given by $J = S_Q + j_q$. For $L = 1$, there are four states with spin-parity $J^P = 0^+$, 1^+, 1^+ and 2^+. If the heavy quark Q is a bottom quark, these states are labelled B_0^*, B_1 for both 1^+ states[1] and B_2^* [2], respectively. The four states, commonly called B_J^*, or alternatively B^{**} [2], are grouped into two sets of degenerate doublets, corresponding to $j_q = 1/2$ and $j_q = 3/2$ as indicated in Table 1. Parity and angular momentum conservation put restrictions on the strong decays of these states to $B^{(*)}\pi$ [3] (see Figure 1). The 0^+ state can only decay to $B\pi$ via an S-wave transition, the $1^+_{1/2}$ to $B^*\pi$ via an S-wave transition, the $1^+_{3/2}$ to $B^*\pi$ via a D-wave transition, and the 2^+ state can decay to both $B\pi$ and $B^*\pi$ via D-wave transitions only. States decaying via an S-wave transition are expected to be much broader than the states decaying via a D-wave transition [3]. In addition to the single pion transitions, decays to $B^*\pi\pi$ and $B\pi\pi$ are also possible. In the case of di-pion transitions, all four B_J^* states are allowed to decay to B^* as well as to B. Although these decays are phase-space suppressed, intermediate states with large width like $B_J^* \to B^{(*)}\rho \to B^{(*)}\pi\pi$ may cause a significant enhancement of the $B^*\pi\pi$ and $B\pi\pi$ final states [4]. Additional B_J^* decay modes with other than one or two accompanying pions are expected to be strongly suppressed but can not be excluded. Therefore, the notations $B^*\pi(X)$ and $B\pi(X)$ are chosen to refer to the final states of B_J^* decays.

Given the HQET predictions listed in Table 1, the four B_J^* states are expected to overlap in mass. So far, in analyses from LEP experiments [5–8] and from CDF [9] B_J^* mesons are reconstructed in the $B\pi$ final state only, observing one single peak in the $B\pi$ mass spectrum. This is not sufficient to resolve any substructure of the four expected B_J^* states. In addition, for decays to $B^*\pi$ where the photon in the decay $B^* \to B\gamma$ is not detected, the reconstructed $B\pi$ mass is shifted by $M_B - M_{B^*} = -46 \text{ MeV}/c^2$. A recent analysis [10] tries to cope with these problems by constraining all properties of the four B_J^* states according to HQET predictions except for the masses and widths of $B_1(1/2)$ and B_2^*.

In this paper a different approach is presented. Using information from the photon in the decay $B^* \to B\gamma$, the $B_J^* \to B^*\pi^\pm(X)$ decays are statistically separated from the $B_J^* \to B\pi^\pm(X)$ decays. This allows a model-independent measurement of the branching ratio $\mathrm{BR}(B_J^* \to B^*\pi(X))$. Assuming that $B^{(*)}\pi X$ decays produce small contributions to the B_J^* width, this method gives insight into the decomposition of the B_J^* into the states allowed to decay to $B\pi$ (B_0^* and B_2^*) from the other states that can only decay to $B^*\pi$.

The $B\pi$ invariant mass spectrum is also fit in the context of HQET expectations. This requires high statistics, extensive background studies and the tagging of the B^* decay. Due to the complexity of the B_J^* signal and its different decay modes, several constraints provided by

---

[1]In the limit $m_Q \to \infty$, the notations $B_1(1/2)$ and $B_1(3/2)$ are used. In the case of mixing of the $J = 1$ states, the notations $B_1(H)$ and $B_1(L)$ are used to distinguish the physical states.

[2]Throughout this paper, we use the Particle Data Group notation B_J^* for orbitally-excited B mesons.

[3]Throughout this paper, $B^{(*)}\pi$ denotes the final states $B\pi$ *and* $B^*\pi$. The notations $B^{(*)}\pi\pi$ and $B^*\pi(X)$ are to be interpreted in the same way.

state	J_j^P	predicted properties [3, 4, 11]			Monte Carlo input	
		mass [GeV/c^2]	width [GeV/c^2]	decay mode	mass [GeV/c^2]	width [GeV/c^2]
B_0^*	$0_{1/2}^+$	5.738	0.20-1.00	$(B\pi)_{S-wave}$	5.750	0.300
B_1	$1_{1/2}^+$	5.757	0.25-1.30	$(B^*\pi)_{S-wave}$	5.770	0.300
B_1	$1_{3/2}^+$	5.719	0.021	$(B^*\pi)_{D-wave}$	5.725	0.020
B_2^*	$2_{3/2}^+$	5.733	0.025	$(B^*\pi)_{D-wave},$ $(B\pi)_{D-wave}$	5.737	0.025

Table 1: Masses, widths and dominant decay modes based on theoretical predictions [3, 4, 11–13] and the corresponding Monte Carlo input values used in the analysis. Recent calculations using a bag model predict widths of $\Gamma(B_0^*) = 0.141$ GeV/c^2 and $\Gamma(B_1(1/2)) = 0.139$ GeV/c^2 for the broad states [14].

HQET are imposed. From the fitting procedure, we obtain model-dependent measurements of the mass and width of $B_1(3/2)$ as well as $BR(B_J^* \to B^*\pi)$.

The paper is organised as follows: the next section describes the data sample and the event simulation. In Section 3, the analysis method is presented. The B reconstruction is described in Section 4. Section 5 contains the photon reconstruction. The pion reconstruction and the total $B\pi$ mass spectrum are presented in Section 6. The $BR(B_J^* \to B^*\pi(X))$ measurement and results from a simultaneous fit to the $B\pi^\pm$ mass spectra of the samples enriched or depleted in the decay $B_J^* \to B^*\pi^\pm(X)$ are presented in Section 7. Systematic uncertainties are evaluated in Section 8. A discussion of the results and conclusions are given in Section 9.

2   Data sample and event simulation

The data used for this analysis were collected from e^+e^- collisions at LEP during 1991–1995, with centre-of-mass energies at and around the peak of the Z^0 resonance. The data correspond to an integrated luminosity of about 140 pb^{-1}. A detailed description of the OPAL detector can be found elsewhere [15, 16].

Hadronic events are selected as described in [17], giving a hadronic Z^0 selection efficiency of $(98.4 \pm 0.4)\%$ and a background of less than 0.2%. A data sample of about 4 million hadronic events is selected. Each event is divided into two hemispheres by the plane perpendicular to the thrust axis and containing the interaction point of the event. The thrust axis is calculated using tracks and electromagnetic clusters not associated with any tracks. To select events within the fiducial acceptance of the silicon microvertex detector and the barrel electromagnetic calorimeter, the thrust axis direction[4] is required to satisfy $|\cos\theta_T| < 0.8$. Monte Carlo simulated samples of inclusive hadronic Z^0 decays are used to evaluate efficiencies and backgrounds. The JETSET 7.4 parton shower Monte Carlo generator [18], with parameters tuned by OPAL [19] and with the fragmentation function of Peterson *et al.* [20] for heavy quarks is used to generate samples of approximately 10 million hadronic Z^0 decays, 2 million $Z^0 \to c\bar{c}$ and 5 million $Z^0 \to b\bar{b}$ decays. The generated events are passed through a program that simulates the response of the OPAL detector [21] before applying the same reconstruction algorithms as

---

[4] In the OPAL coordinate system, the x axis points towards the centre of the LEP ring, the y axis points upwards and the z axis points in the direction of the electron beam. θ and ϕ are the polar and azimuthal angles, and the origin is taken to be the centre of the detector.

for data. All generated Monte Carlo samples contain $L = 1$ states for bottom and charmed mesons, as well as vector meson partners of the ground states. The generated production rates, masses and widths of all resonant states are consistent with experimental measurements when available and with theoretical predictions elsewhere (see also Table 1).

3   Analysis overview

The analysis is based on the reconstruction of B* in the Bγ final state and a separate reconstruction of B$_J^*$ in the B$\pi^\pm$ final state. A direct reconstruction of B$_J^*$ decaying to B*π, B* $\to$ Bγ giving B$\gamma\pi^\pm$ in the final state is inappropriate because of the large combinatorial background and the insufficient detector resolution. Therefore, our approach employs a statistical separation of B$_J^* \to$ B*$\pi^\pm(X)$ from B$_J^* \to$ B$\pi^\pm(X)$ decays.

B mesons produced in Z$^0 \to$ b$\overline{\text{b}}$ events are reconstructed inclusively to achieve high efficiency. No attempt is made to reconstruct specific B decay channels. On the contrary, properties common to all weakly decaying b hadrons are used for the B reconstruction. For each B candidate, a weight $\mathcal{W}(\text{B}^*)$ is formed where $\mathcal{W}(\text{B}^*)$ represents the probability for the B to have come from a B*. The probability $\mathcal{W}(\text{B}^*)$ is based on the reconstruction of photon conversions and of photons detected in the electromagnetic calorimeter. All B candidates are then combined with charged pions to form B$_J^*$ meson candidates. Using the weight $\mathcal{W}(\text{B}^*)$, we derive two mutually exclusive subsamples of B$\pi^\pm$ combinations, one enriched and the other depleted in its B* content. Invariant B$\pi^\pm$ mass distributions are formed for both samples. The shape of the non-B$_J^*$ background of the two distributions is taken from Monte Carlo simulation and normalised to the data in the upper sideband region and subtracted from the corresponding data distributions. The branching ratio BR(B$_J^* \to$ B*$\pi(X)$) is obtained from the observed number of B$_J^*$ and the different efficiencies for B$_J^* \to$ B*$\pi^\pm(X)$ and B$_J^* \to$ B$\pi^\pm(X)$ decays in the B*-enriched and the B*-depleted samples. Applying a simultaneous fit to the Bπ mass spectra of both samples several details of the B$_J^*$ four-state composition and of the B$_J^*$ decay modes are extracted.

Whereas the BR(B$_J^* \to$ B*$\pi(X)$) result obtained from counting the number of B$_J^*$ signal entries of the samples enriched or depleted in the decay B$_J^* \to$ B*$\pi^\pm(X)$ is model-independent and does not rely on the shape of the Bπ signal, the fit to the Bπ mass spectra makes use of HQET assumptions on the composition and the decay modes of the B$_J^*$ signal.

4   Selection and reconstruction of B mesons

B mesons are reconstructed using an extended version of the method used in earlier analyses [5, 22]. Since the reconstructed B mesons are used to form B* and B$_J^*$ candidates, the B reconstruction is tuned to minimise the uncertainties on the B direction and energy, while maintaining a high reconstruction efficiency.

4.1   Tagging of Z$^0 \to$ b$\overline{\text{b}}$ events

To achieve optimal b-tagging performance, each event is forced to a 2-jet topology using the Durham jet-finding scheme [23]. In calculating the visible energies and momenta of the event and of individual jets, corrections are applied to prevent double counting of energy in the case of tracks with associated clusters [24]. A b-tagging algorithm is applied to each jet using three

independent methods: lifetime tag, high p_T lepton tag and jet-shape tag. A detailed description of the algorithm can be found in [25]. The b-tagging discriminants calculated for each of the jets in the event are combined to yield an event b likelihood $\mathcal{B}_{\text{event}}$. For each event, $\mathcal{B}_{\text{event}} > 0.6$ is required. After this cut, the $Z^0 \to b\bar{b}$ event purity is about 96%. The cut on the direction of the event thrust axis, $|\cos\theta_T| < 0.8$, as described in Section 2, removes roughly a quarter of all $Z^0 \to b\bar{b}$ events and after the cut on $\mathcal{B}_{\text{event}}$, the total b event tagging efficiency with respect to all produced $Z^0 \to b\bar{b}$ events is about 49%, where these numbers are obtained from Monte Carlo simulation. At this stage, about 750 000 b hadron candidates are selected.

4.2 Reconstruction of B energy and direction

The primary event vertex is reconstructed using the tracks in the event constrained to the average position and effective spread of the e^+e^- collision point. For the b hadron reconstruction, tracks and electromagnetic calorimeter clusters with no associated track are combined into jets using a cone algorithm [26] with a cone half-angle of 0.65 rad and a minimum jet energy of 5.0 GeV [5]. The two most energetic jets of each event are assumed to contain the b hadrons. For each jet we reconstruct the energy and direction.

In each hemisphere defined by the jet axis, a weight is assigned to each track and each cluster, where the weight corresponds to the probability that any one track or cluster is a product of the b hadron decay. The b hadron is reconstructed by summing the weighted momenta of the tracks and clusters. The reconstruction algorithm is applied to all b hadron species and is 100% efficient. Since this analysis aims at the reconstruction of $B_{u,d}$ mesons which make up about 80% of the b hadron sample, b hadron candidates are referred to as B mesons in the following. Details of the reconstruction method are provided below.

4.2.1 Calculation of track weights

Two different types of weights are assigned to each track:

- ω_{vtx}, calculated from the impact parameter significances of the track with respect to both the primary and secondary vertices;

- ω_{NN}, the output of a neural network based on kinematics and track impact parameters with respect to the primary vertex.

The calculation of ω_{vtx} requires the existence of a secondary vertex, whereas ω_{NN} does not and is therefore available for all tracks. The search for detached secondary vertices proceeds as follows:

Each jet is searched for secondary vertices using a vertexing algorithm similar to that described in [5], making use of the tracking information in both the $r - \phi$ and $r - z$ planes if available. If a secondary vertex is found, the primary vertex is re-fitted excluding the tracks assigned to the secondary vertex. Secondary vertex candidates are accepted and called 'good' secondary vertices if they contain at least three tracks and have a decay length greater than 0.2 mm. If there is more than one good secondary vertex attached to a jet, the vertex with the largest number of significant[6] tracks is taken. If there is a tie, the secondary vertex with the

---

[5]The cone jet-finder provides the best b hadron energy and direction resolution compared to other jet finders studied here.

[6]A track is called significant if its impact parameter significance with respect to the primary vertex is larger than 2.5.

larger separation significance with respect to the primary vertex is taken. If a good secondary vertex is determined, a weight is calculated for each track in the hemisphere of the jet using the impact parameter significance of the track with respect to both the primary and secondary vertices. This weight is given by

$$\omega_{\text{vtx}} = \frac{R(b/\eta)}{R(b/\eta) + R(d/\sigma)} , \qquad (1)$$

where b and η are the impact parameter and its error with respect to the secondary vertex, and d and σ are the same quantities with respect to the primary vertex. R is a symmetric function describing the impact parameter significance distribution with respect to a fitted vertex. The ω_{vtx} distribution for tracks of hemispheres with a good secondary vertex is shown in Figure 2a and compared with the corresponding Monte Carlo distribution. The weight ω_{vtx} shows a weak correlation with the momentum of the track.

For each track, the weight ω_{NN} is calculated using an artificial neural network [27] trained to discriminate b hadron decay products from fragmentation tracks in a jet. The neural network was trained using as inputs the scaled track momentum $x_p = p/E_{\text{beam}}$, the track rapidity relative to the estimated B direction, the impact parameters of the track with respect to the primary vertex in the $r - \phi$ and $r - z$ planes and the corresponding errors on the impact parameters [28]. As a preliminary estimate, the jet axis is taken as the estimated B direction. The ω_{NN} distribution is shown in Figure 2b. If a good secondary vertex exists, the track weight ω_{NN} is combined with the vertex weight ω_{vtx} using the prescription

$$\omega_{\text{tr}} = \frac{\omega_{\text{NN}} \cdot \omega_{\text{vtx}}}{(1 - \omega_{\text{NN}}) \cdot (1 - \omega_{\text{vtx}}) + \omega_{\text{NN}} \cdot \omega_{\text{vtx}}} . \qquad (2)$$

The weight ω_{tr} in Equation 2 is approximately the probability that the track is a b hadron decay product. In the case where there is no good secondary vertex in the jet, the total track weight ω_{tr} is simply given by $\omega_{\text{tr}} = \omega_{\text{NN}}$. The combined weight ω_{tr} for tracks of all hemispheres is shown in Figure 2c.

4.2.2 Calculation of cluster weights

Similar weights are calculated for energy clusters reconstructed in the electromagnetic and hadronic calorimeters to represent the probability the clusters came from a B hadron decay. Weights ω_{ecl} and ω_{hcl} are assigned to each electromagnetic and hadronic cluster in the hemisphere of the B meson based on their rapidity with respect to the estimated B direction. The weight is equal to the probability, calculated using the Monte Carlo simulation as a function of the cluster energy, that the cluster came from the decay of a B meson. Clusters associated with a track have the estimated energy of the track subtracted.

4.2.3 Calculation of B direction

The B momentum is calculated iteratively by a weighted sum of all tracks and clusters in the hemisphere:

$$\vec{p} = \sum_{i=1}^{N_{\text{track}}} \omega_{\text{tr},i} \cdot \vec{p}_i + \sum_{i=1}^{N_{\text{ecal}}} \omega_{\text{ecl},i} \cdot \vec{p}_i + \sum_{i=1}^{N_{\text{hcal}}} \omega_{\text{hcl},i} \cdot \vec{p}_i \qquad (3)$$

where N_{track}, N_{ecal} and N_{hcal} denote the number of tracks, electromagnetic clusters and hadronic clusters, respectively. The rapidity calculation, for both tracks and clusters, is initially per-

formed relative to an estimate of the B meson direction[7]. The weights are then recalculated with the rapidity determined using the new B direction estimate.

An estimate of the B hadron direction is made for all B candidates based on the weighted momentum sum of the tracks and clusters in the jet. In addition, the vector from the primary vertex to the secondary vertex yields an estimate of the B direction for those jets where a good secondary vertex has been identified. When both estimates are available the weighted average is taken, using the calculated uncertainties of each direction estimate. The covariance matrices of the primary and secondary vertices determine the error on the B flight direction. The error on the momentum sum is estimated by removing each term in turn from the sum in Equation 3, calculating the change in the B direction caused by this omission and adding up in quadrature the corresponding error contributions from each track and cluster. The final estimate of the B direction is obtained by taking the error-weighted sum of the B direction calculated with the momentum sum method and the B direction obtained from the primary and secondary vertex positions. The direction information in the $r - z$ plane of the secondary vertex is only used if the vertex is built with tracks that left at least four hits in the z-layers of the silicon microvertex detector (the maximum number of these hits per track is two).

The error $\Delta\alpha$ on the weighted sum of both B direction estimators described in the previous paragraph is a measure for the quality of the B direction[8]. To improve the resolution on the B direction, which in turn dominates the Bπ mass resolution, a cut on $\Delta\alpha$ is imposed. Since this analysis aims at a separation of some of the B$_J^*$ states by reconstructing different B$_J^*$ decay channels rather than obtaining a very good Bπ mass resolution, the cut $\Delta\alpha < 0.035$ is rather loose. This cut removes the 20% of the B candidates with the poorest direction resolution, mainly those with no associated good secondary vertex.

4.2.4 Calculation of B energy

The resolution on the total energy of the B candidate can be significantly improved by constraining the total centre-of-mass energy, E_{CM}, to twice the LEP beam energy. Assuming a two-body decay of the Z^0, we obtain:

$$E_{\mathrm{B}} = \frac{E_{\mathrm{CM}}^2 - M_{\mathrm{recoil}}^2 + M_{\mathrm{B}}^2}{2E_{\mathrm{CM}}} \,, \tag{4}$$

where the mass of the b hadron is set to the B meson mass $M_{\mathrm{B}} = 5.279$ GeV/c^2 and M_{recoil} denotes the mass recoiling against the B meson. The recoil mass and the recoil energy E_{recoil} are calculated by summing over all tracks and clusters[9] of the event weighted by $(1 - \omega_i)$ and assuming the particle masses used in the calculation of E_i. To account for the amount of undetected energy mainly due to the presence of neutrinos, the recoil mass is scaled by the ratio of the expected energy in the recoil to the energy actually measured:

$$M_{\mathrm{recoil,new}} = M_{\mathrm{recoil,old}} \cdot \frac{E_{\mathrm{CM}} - E_{\mathrm{B}}}{E_{\mathrm{recoil}}} \tag{5}$$

where E_{B} is taken from Equation 4. The new recoil mass value $M_{\mathrm{recoil,new}}$ obtained from Equation 5 is substituted into Equation 4 and the calculation of E_{B} is iterated. After two

---

[7] The initial input for this axis is the jet direction calculated using tracks and unassociated electromagnetic clusters.

[8] In the case where no good secondary vertex exists, $\Delta\alpha$ is simply given by the uncertainty on the momentum sum.

[9] Tracks and clusters not contained in the hemisphere of the B meson candidate have weights $\omega_i = 0$. ω_i denotes the weight $\omega_{\mathrm{tr},i}$, $\omega_{\mathrm{ecl},i}$ and $\omega_{\mathrm{hcl},i}$ for tracks, electromagnetic clusters and hadronic clusters, respectively.

iterations the uncertainty on the B meson energy is minimised. A minimum B energy of 15 GeV is required to further improve the energy resolution.

After all these cuts, the narrower Gaussian from a two Gaussian fit to the difference between the reconstructed and generated B meson energy has $\sigma = 2.3$ GeV, and 86% of the entries are contained within 3σ. The distribution of the difference between the reconstructed and generated ϕ angle of simulated B mesons can be described by a similar fit. The standard deviation of the narrower Gaussian is 14.2 mrad and 88% of the entries lie within 3σ. The corresponding quantities describing the θ resolution are $\sigma = 15.0$ mrad and 89%, respectively.

The complete B meson selection applied to the full data sample results in $574\,288$ tagged jets with a b purity of about 96%, as estimated from Monte Carlo. About 75% of the selected jets contain a good secondary vertex.

5   The decay $\mathrm{B}^* \to \mathrm{B}\gamma$

The photon produced in the decay $\mathrm{B}^* \to \mathrm{B}\gamma$ has an energy of about 46 MeV in the rest frame of the B^*. The mean energy of the photon in the laboratory frame is approximately 350 MeV, with a maximum energy below 800 MeV. Due to the kinematics of the process, these photons are produced predominantly in the core of the jet. The high particle density in this region gives rise to a high background level when identifying the photon. Since a high B^* reconstruction efficiency is crucial for this analysis, photons are reconstructed in two ways: from energy deposits in the electromagnetic calorimeter and from converted photons in the tracking volume. The conversion probability within the OPAL tracking system for photons coming from the decay $\mathrm{B}^* \to \mathrm{B}\gamma$ is approximately 8%.

5.1   Reconstruction of photon conversions

The reconstruction of converted photons is optimised for the low energy region. The selection algorithm is partially based on quantities that have been used in earlier analyses [29] but tuned to obtain high efficiency rather than very good angular and momentum resolution. Given the low energy carried by these photons, we ignore calorimetry information and only use tracking information for the reconstruction of converted photons.

Tracks with a total momentum p below 1.0 GeV/c, opposite charge assignment and a measured $\mathrm{d}E/\mathrm{d}x$ within three standard deviations of the expected value for electrons are combined into pairs. For each pair, the track with the greater scalar momentum is required to have a transverse momentum $p_t > 50$ MeV/c with respect to the beam axis and at least 20 hits in the central jet chamber. For the track with lower momentum, a minimum p_t of 20 MeV/c is required. The asymmetric selection cuts for the two tracks in a pair guarantee at least one well measured track and reflect the fact that the electron and the positron of a converted photon tend to have different momenta in the laboratory frame. To suppress random track combinations, the distance of closest approach between the two tracks of a pair in the $r - \phi$ plane has to be smaller than 1.0 cm with an opening angle between the tracks at their point of closest approach smaller than 1.0 rad.

In order to make optimal use of all the available information, the following measured quantities for each conversion track pair candidate are fed into a neural network:

- the distance of closest approach between the two tracks in the $r - \phi$ plane;

- the radial distance with respect to the z axis of the first and last measured hits in the inner tracking chambers for each track;

- the radial distance with respect to the z axis of the common vertex[10] of both tracks obtained from a fit in the $r - \phi$ plane;

- the impact parameter with respect to the primary vertex in the $r - \phi$ plane of the reconstructed photon;

- the invariant mass of the track pair assuming both tracks to be electrons;

- the transverse momentum relative to the z axis of the lower momentum track.

All conversion candidates with a neural network output greater than 0.7 and a photon energy below 1.5 GeV are called 'good' conversion candidates for a given B meson candidate if the opening angle between the reconstructed B momentum vector and the reconstructed photon momentum vector is smaller than 90°. At this stage, an average of 0.82 good conversion candidates is selected per B candidate in both data and Monte Carlo. The candidate multiplicity distributions are shown in Figure 3a. The total efficiency to detect photons from the decay $B^* \to B\gamma$ with the conversion algorithm is estimated from simulation to be $(2.70 \pm 0.01_\text{stat})\%$. The efficiency is rather independent of the photon energy from 1.0 GeV down to 200 MeV where it rapidly drops to zero due to track selection requirements. The amount of fake conversions in the selected sample is estimated from Monte Carlo simulation to be $(11.75 \pm 0.04_\text{stat})\%$.

Fits to the difference between the reconstructed and generated photon energy in Monte Carlo are made using the sum of two Gaussians, both constrained to the same mean value. The narrower Gaussian has a standard deviation of 5 MeV at an energy of 200 MeV, and rises to 13 MeV at an energy of 750 MeV, and about 70% of the entries are contained within 3σ. Similar fits to the ϕ and θ resolutions give values of 3.4 mrad (70%) and 5.4 mrad (61%), respectively.

5.2   Reconstruction of photons in the electromagnetic calorimeter

Photons are also detected as showers in the barrel region of the electromagnetic calorimeter. The location and energy of these showers are obtained from a fit to the energy deposits in the individual lead glass blocks not associated with any track. The whole reconstruction method has been shown to work in the dense environment of hadronic jets down to photon energies as low as 150 MeV. The details of the reconstruction are given in [30].

Showers in the electromagnetic calorimeter are accepted as photon candidates if they have an energy in the range 200 MeV to 850 MeV and a photon probability $P_\gamma > 0.20$, where P_γ is the output of a simplified neural network [30]. If the opening angle between such a shower and a reconstructed B candidate is less than 90°, this shower is considered a 'good' photon candidate for the corresponding B candidate. On average, there are 4.59 (4.38) good calorimeter photon candidates per B candidate selected in the data (Monte Carlo) sample. To correct for the observed discrepancy, the Monte Carlo is reweighted to the data distribution shown in Figure 3b. The efficiency to detect a photon from the decay $B^* \to B\gamma$ in the electromagnetic calorimeter is estimated to be $(14.52 \pm 0.03_\text{stat})\%$ using Monte Carlo simulated events. The fraction of fake photons arising from tracks and neutral hadrons in the sample ranges from

---

[10]The z position of this vertex is fitted independently and the reconstructed photon vector is constrained to the z coordinate of the primary vertex to improve the accuracy of the θ determination.

32% at a photon energy of 850 MeV up to 43% at a photon energy of 200 MeV. If compared with the selected conversion sample, the selection of $B^* \rightarrow B\gamma$ photons in the electromagnetic calorimeter has a much higher efficiency but lower purity.

As with the converted photons, the energy resolution has been determined from Monte Carlo simulation using a double Gaussian fit. The narrower Gaussian has a width of 20 MeV at a photon energy of 250 MeV and increases up to 86 MeV at an energy of 800 MeV, and about 75% of the entries are contained within 3σ. Similar fits to the ϕ and θ resolutions give values of 3.6 mrad (65%) and 3.6 mrad (72%), respectively. In contrast to the conversion sample, photons reconstructed in the electromagnetic calorimeter have much higher energy uncertainties, but a better θ resolution.

5.3 Reconstruction of $B^* \rightarrow B\gamma$ decays

Each reconstructed B meson candidate is combined with all good conversion and calorimeter candidates to reconstruct B^* candidates. The invariant mass of a $B\gamma$ combination is defined as

$$M_{B\gamma} = \sqrt{M_B^2 + 2E_B E_\gamma - 2p_B 2p_\gamma \cos\alpha} \quad , \tag{6}$$

where M_B is 5.279 GeV/c^2 and α is the measured angle between the B meson and the photon candidate. The mass difference $\Delta M = M_{B\gamma} - M_B$ between the B^* candidate and the B is calculated by simply subtracting the nominal B mass of $M_B = 5.279$ GeV/c^2 from $M_{B\gamma}$.

The mass difference distributions of the conversion sample observed in the data and the corresponding Monte Carlo background are shown in Figure 4a. The background is normalised to the data in the sideband region 0.09 GeV/c^2 < ΔM < 0.20 GeV/c^2. The background subtracted signal of Figure 4b is fitted to the sum of two Gaussians fixed to the same mean, where one of the Gaussians is allowed to have asymmetric width. The observed asymmetry of the mass resolution of the conversion sample is well simulated in the Monte Carlo and is due to the very loose track requirements of the lower momentum track of the conversion pair. A mass difference of $\Delta M = (45.87 \pm 0.25_{\text{stat}})$ MeV/c^2 is obtained from the fit to the data, where the error is statistical only. This result agrees well with the current world average value of (45.78 ± 0.35) MeV/c^2 [2].

The ΔM distribution using calorimeter photons is shown in Figure 5a. The background is taken from Monte Carlo simulation and normalised to the data in the sideband region 0.10 GeV/c^2 < ΔM < 0.20 GeV/c^2. The same fit function as for the photon conversion sample is used to obtain the mass difference ΔM from the background subtracted signal distribution in Figure 5b. A value of $(47.30 \pm 0.61_{\text{stat}})$ MeV/c^2 is obtained from this fit, which is consistent within two sigma with the result from the fit to the conversion signal.

For the B^* sample reconstructed with photon conversions, the mass resolution is dominated by the uncertainty on the reconstructed B direction. For the calorimeter photon sample, the B^* mass resolution suffers in addition from the energy resolution of the calorimeter. Due to the high background of fake photons and the moderate energy resolution at low photon energies, the signal-to-background ratio is rather poor for calorimeter photons. Therefore, uncertainties in the B^* reconstruction using these photons are dominated by systematic errors on the background shape and energy calibration. All systematic uncertainties arising from the B^* reconstruction will be discussed in Section 8.

5.4 The B* probability $\mathcal{W}(\mathrm{B}^*)$

To select samples enhanced and depleted in B* mesons, a B* probability is assigned to each B candidate. This probability combines information from both conversion and calorimeter photon candidates and represents the probability that a B candidate is the true daughter of a B* meson. Only the best conversion and best calorimeter candidate assigned to any one B candidate are considered in the calculation of this probability, where the best candidate is defined as that which gives $\Delta M = M_{\mathrm{B}\gamma} - M_{\mathrm{B}}$ closest to the world average of 45.78 MeV/c^2 [2].

This weight is constructed by parametrising the purity of the mass difference distribution in several variables in Monte Carlo simulation. For calorimeter photon candidates, this parametrisation is performed as a function of the photon probability, P_γ (see Section 5.2), and the total number of good calorimeter photon candidates found per B candidate. For each B candidate, a single weight is calculated by taking the simple mean of the weight resulting from each of the above parametrisations.

Similarly, for conversion photon candidates, the parametrisation is performed in ΔM as a function of the total number of conversion candidates, and a weight is extracted as for the calorimeter candidates. The two weights obtained from conversion and calorimeter photons are combined by taking their mean.

The resulting weight $\mathcal{W}(\mathrm{B}^*)$ is shown in Figure 6a for Monte Carlo and data, and the contributions from jets containing a B* and jets containing no B* as seen in the simulation are shown. The primary features of the $\mathcal{W}(\mathrm{B}^*)$ distribution are:

- a peak at $\mathcal{W}(\mathrm{B}^*) = 0.625$, corresponding to B candidates with no associated good conversion or calorimeter photon candidate;

- a peak at $\mathcal{W}(\mathrm{B}^*) = 0.632$, containing B candidates with no good conversion candidate and a best calorimeter candidate having a Bγ mass far away from the nominal B* mass;

- a peak around $\mathcal{W}(\mathrm{B}^*) = 0.656$, containing B candidates with the best calorimeter candidate close to the nominal B* mass;

- a peak at $\mathcal{W}(\mathrm{B}^*) = 0.715$, containing B candidates with the best calorimeter candidate being close to the nominal B* mass and having a high photon probability P_γ;

- the tail towards high B* probabilities is made up by best conversion candidates very close to the nominal B* mass.

The assignment of the specific photon candidate samples to the peaks and to the tail of the $\mathcal{W}(\mathrm{B}^*)$ distribution is based on Monte Carlo information. Figure 6b shows the ratio $\varepsilon(\mathrm{B}^*)/\varepsilon(\mathrm{B})$ versus $\mathcal{W}(\mathrm{B}^*)$. $\varepsilon(\mathrm{B}^*)$ refers to the efficiency to select a B meson from a true $\mathrm{B}^* \to \mathrm{B}\gamma$ decay and $\varepsilon(\mathrm{B})$ is the efficiency to select a B meson which has not come from a B*. In general, the Monte Carlo simulation of $\mathcal{W}(\mathrm{B}^*)$ describes the data adequately. A comparison of the Monte Carlo and data distributions yields a χ^2 per degree of freedom of two. A cut on $\mathcal{W}(\mathrm{B}^*)$ allows the production of samples of B candidates with different B* fractions. Further details and systematic studies concerning $\mathcal{W}(\mathrm{B}^*)$ are given in Section 8.

6 Reconstruction of orbitally-excited B mesons

All B_J^* candidates, even those expected to decay into $\mathrm{B}^*\pi^\pm$, are reconstructed using the measured four-momenta of the B meson and the pion. B candidates are selected and reconstructed

as described in Section 4 and combined with charged pion candidates. Pions produced in the decay of a B_J^* will be referred to as 'signal pions'. Since the B_J^* decays strongly, signal pions are expected to be associated to the primary event vertex rather than to a possible secondary vertex. In comparison with other pions created in the fragmentation process, signal pions are expected to have a large longitudinal momentum p_l with respect to the jet axis. These are the basic characteristics used to separate signal pions from B decay products and from fragmentation tracks. A significant number of non-resonant fragmentation pions are expected to be produced near a B meson. The kinematics of these pions is similar to the signal pions, giving rise to a combinatorial background in the invariant mass of $B\pi$ candidates. Tracks from B decay also contribute to the background due to the inability to unambiguously associate all B decay tracks with the secondary vertex.

6.1   Pion selection

The signal pion selection for this analysis makes use of techniques used in [5] and [8]. All tracks that are well measured according to a standard track selection [31] are considered as possible signal pion candidates if they belong to the same jet as the B candidate. Additionally, the following selection cuts are applied in the given order:

- The measured ionisation energy loss dE/dx has to be consistent with the expected value for pions within 2.6 standard deviations, if dE/dx information is available for this track.

- To suppress B decay tracks, the track weight ω_{NN} as described in Section 4.2 has to be smaller than 0.9.

- The B decay track rejection is improved by the requirement $\omega_{\mathrm{NN2}} < 0.7$, where ω_{NN2} is a neural network output defined for jets containing a secondary vertex. The inputs for ω_{NN2} are similar to the inputs for ω_{NN}, but also the impact parameter significances in the $x - y$ and the z plane with respect to the secondary vertex are used.

- From all tracks that pass the previous selection criteria, only the one with the highest longitudinal momentum with respect to the jet axis, p_l^{max}, is kept for each B candidate,

- A reduction of B decay track background in the p_l^{max} sample is obtained by the requirements $\omega_{\mathrm{NN}} < 0.80$ and $\omega_{\mathrm{NN2}} < 0.50$ [11].

- Fragmentation tracks in the p_l^{max} sample are removed with the requirement $\omega_{\mathrm{NN}} > 0.20$. Since ω_{NN} is designed to achieve optimal separation of b hadron decay tracks from fragmentation tracks using impact parameter information *and* kinematics, the Monte Carlo indicates a fairly flat ω_{NN} distribution for signal pions. On the contrary, fragmentation tracks peak at zero.

- A momentum of $p > 1.0$ GeV/c is required for signal pion candidates. In the simulation, the momentum distribution of signal pions has a mean value of 2.9 GeV/c with an RMS of 1.3 GeV/c before the cut is applied. The B_J^* mass spectrum for single pion transitions is not influenced by the momentum requirement.

---

[11]If no secondary vertex is present in the jet, the cut $\omega_{\mathrm{NN}} < 0.50$ instead of $\omega_{\mathrm{NN2}} < 0.50$ is applied.

6.2 Bπ± mass spectrum

The signal pion candidate passing the selection cuts described in Section 6.1 is combined with the corresponding B candidate to form a B_J^* candidate. The invariant mass is calculated using Equation 6 as for the B^* mass, where the photon is replaced by a pion and the appropriate pion mass term is added. The cuts of the signal pion selection have been chosen to obtain an acceptable signal-to-background ratio at high signal efficiency. The order of the non-commuting selection requirements using ω_{NN}, ω_{NN2} and p_l^{max} aims to maximise the difference between the shape of the signal and background contributions to the $M_{B\pi}$ distribution.

Due to the intrinsic widths of the B_J^* states and the limited detector resolution, only a single peak is seen in the $M_{B\pi}$ spectrum of Figure 7a on top of the combinatorial background. According to the simulation, the $M_{B\pi}$ resolution can be described by the sum of a narrow Gaussian and an asymmetric Gaussian, both constrained to the same mean value (see Figure 8). The mass resolution depends linearly on $M_{B\pi}$. In the B_J^* signal region around 5.7 GeV/c^2, the standard deviation of the narrow Gaussian is $\sigma = 33$ MeV/c^2, and 85% of the resolution function entries are contained within 3σ. The reliability of the simulated B meson energy and direction resolution which dominate the $B\pi$ mass resolution is proven by a well simulated shape and peak position of the B^* signal using the conversion photon sample (see Section 5).

The Monte Carlo combinatorial background is checked against data using different test samples strongly enhanced in each of the following physics background sources: 1) Fake B_J^* candidates from light and charm quark events; 2) Fake B_J^* arising from true b hadrons combined with a pion from the weak decay of the b hadron itself; 3) Fake B_J^* formed by combining true b hadrons with fragmentation tracks which have not come from a B_J^* resonance. The simulation indicates that each test sample is strongly enhanced in the background source under study and that the B_J^* signal is suppressed by about a factor of eight compared to the original B_J^* signal selection. The $B\pi$ mass distributions of the background samples in data are compared with the corresponding Monte Carlo mass distributions (see also Section 8.1.2). In the case of a significant deviation, the simulated background is reweighted to the data. The Monte Carlo background distribution so obtained is fitted using a threshold function of the form

$$C_1 \cdot \sqrt{x - (m_B + m_\pi)} \cdot \left(\Phi \left(\frac{x - C_2}{C_3} \right) \right)^{C_4} \quad , \qquad (7)$$

where Φ is the Landau density function[12]. This background function gives a good empirical fit with only four free parameters C_i. The fitted Monte Carlo background is normalised in the sideband region 6.10 GeV/$c^2 < M_{B\pi} <$ 7.10 GeV/c^2 and subtracted from the data distribution. The obtained B_J^* signal is shown in Figure 7b.

The reconstruction efficiency for B_J^* depends on the reconstructed mass $M_{B\pi}$. Monte Carlo studies indicate that the efficiency stays constant at high $M_{B\pi}$ values down to $M_{B\pi} =$ 5.7 GeV/c^2. Below 5.7 GeV/c^2, the reconstruction efficiency becomes smaller as $M_{B\pi}$ decreases, mainly due to the p_l^{max} requirement. At the $B\pi$ mass threshold, the signal efficiency is close to zero. The B_J^* distribution of Figure 7b is corrected for efficiency and the resulting signal is shown in Figure 7c.

The mean mass, shape and yield of the observed B_J^* signal is roughly in agreement with other measurements [5–8]. The structure of the $B\pi^\pm$ mass spectrum is too broad to stem from a single resonance and leaves room for interpretation. The peak is expected to contain two broad and two narrow B_J^* states, and part of the true mass spectrum is shifted to lower mass

---

[12] $\Phi(\lambda) = \frac{1}{2\pi i} \int_{c-i\infty}^{c+i\infty} e^{\lambda s + \ln s} ds$

values by 46 MeV/c^2 due to the omission of the photon in the reconstruction of $B_J^* \to B^*\pi$ decays. The peak may also include a small fraction of B_{sJ}^* due to the misidentification of kaons as pions. In addition, the peak may contain contributions from $B_J^* \to B^{(*)}\pi X$ giving rise to satellite peaks in the region 5.4 GeV/c^2 < $M_{B\pi}$ < 5.6 GeV/c^2, since X is not included in the invariant mass calculation. If broad B_J^* states have masses close to the $B\pi$ threshold, they have an asymmetric signal shape due to phase-space suppression. Radially-excited B mesons (2S) in the decay channels $B^{(*)\prime} \to B^{(*)}\pi$ and $B^{(*)\prime} \to B^{(*)}\pi\pi$ may contribute, although the production rate of $B^{(*)\prime}$ is assumed to be small compared to the B_J^* production rate according to [10] and [32]. Since there are several ambiguities, e.g. due to $B_J^* \to B^{(*)}\pi\pi$, $B^{(*)\prime}$ decays and uncertainties in the combinatorial background, further details of the signal can only be obtained by making additional, model-dependent assumptions.

7 B_J^* transitions to B^* and to B

In this section, information from the reconstructed $B\pi^\pm$ mass is combined with the weight $\mathcal{W}(B^*)$. The total B_J^* sample is divided into two samples, one enriched and one depleted in the decay $B_J^* \to B^*\pi(X)$, by applying a cut on $\mathcal{W}(B^*)$, as indicated in Figure 6a. These two B_J^* samples allow a model-independent measurement of the ratio $BR(B_J^* \to B^*\pi(X))$, where no distinction between decays to $B^*\pi$ and $B^*\pi X$ is possible. Also a fit with $BR(B_J^* \to B^*\pi)$ as an additional free fit parameter is performed. In this fit, only $B_J^* \to B^{(*)}\pi$ and $B_J^* \to B^{(*)}\pi\pi$ decays are considered. The fit result of the branching ratio $BR(B_J^* \to B^*\pi)$ does *not* include the $B^*\pi\pi$ final state as the sensitivity of the fit is negligible for di-pion transitions of the B_J^*.

7.1 Model-independent measurement of $BR(B_J^* \to B^*\pi(X))$

The branching ratio $BR(B_J^* \to B^*\pi(X))$ is obtained by counting the number of signal entries of the B_J^* samples enriched or depleted in the decay $B_J^* \to B^*\pi^\pm(X)$. The cut value on $\mathcal{W}(B^*)$ is chosen to minimise the uncertainty of the measurement. The statistical error on $BR(B_J^* \to B^*\pi(X))$ is minimal if both subsamples are of the same size. Systematic uncertainties in the $B\pi^\pm$ background have minimal impact on $BR(B_J^* \to B^*\pi(X))$ if the signal-to-background ratio is the same for the $B\pi^\pm$ mass distributions of the B^*-enriched and the B^*-depleted samples. The optimal cut on $\mathcal{W}(B^*)$ is 0.648, fulfilling the minimal systematic error requirement and coming as close as possible to the minimum statistical error requirement (see Figure 6).

The B^* enrichment and depletion method can be evaluated by the different selection efficiencies for the transitions $B_J^* \to B^*\pi^\pm$ and $B_J^* \to B\pi^\pm$ in the B^*-enriched and B^*-depleted samples. With the definitions

- $\varepsilon_{\rm E}^*$: $B_J^* \to B^*\pi$ efficiency of B^*-enriched sample;

- $\varepsilon_{\rm D}^*$: $B_J^* \to B^*\pi$ efficiency of B^*-depleted sample;

- $\varepsilon_{\rm E}$: $B_J^* \to B\pi$ efficiency of B^*-enriched sample;

- $\varepsilon_{\rm D}$: $B_J^* \to B\pi$ efficiency of B^*-depleted sample;

- efficiency ratios : $e_0 = \varepsilon_{\rm D}/\varepsilon_{\rm E}^*$; $e = \varepsilon_{\rm E}/\varepsilon_{\rm D}$; $e^* = \varepsilon_{\rm D}^*/\varepsilon_{\rm E}^*$,

we calculate from Monte Carlo the efficiency values presented in Table 2. The numbers reflect the cut on $\mathcal{W}(B^*)$ and thus the quality of the B^* enrichment versus the B^* depletion. Only the

efficiency ratios given in the right column of Table 2, not the absolute efficiencies, are needed for the determination of $\mathrm{BR}(\mathrm{B}_J^* \to \mathrm{B}^*\pi(X))$. For the $\mathrm{BR}(\mathrm{B}_J^* \to \mathrm{B}^*\pi(X))$ measurement, the

efficiency		efficiency ratio	
$\varepsilon_{\mathrm{E}}^*$	0.05084 ± 0.00023	e_0	1.566 ± 0.010
$\varepsilon_{\mathrm{D}}^*$	0.06680 ± 0.00026	e	0.578 ± 0.005
ε_{E}	0.04601 ± 0.00030	e^*	1.314 ± 0.008
ε_{D}	0.07962 ± 0.00039		

Table 2: Efficiencies for the reconstruction of B_J^* decaying to $\mathrm{B}^*\pi$ and to $\mathrm{B}\pi$. The numbers are calculated with respect to the total number of B_J^* passing the B selection in the Monte Carlo. Therefore, the numbers reflect the effect of the cut on $\mathcal{W}(\mathrm{B}^*)$ and the charged pion selection. Also a factor of 2/3 assuming isospin symmetry to account for decays of B_J^* via neutral pions is included in each of the efficiency values. The errors are statistical only.

invariant $\mathrm{B}\pi^\pm$ mass distributions of the B^*-enriched and the B^*-depleted sample are used. Both mass distributions are independent subsamples of the distribution shown in Figure 7, but contain different compositions of $\mathrm{B}_J^* \to \mathrm{B}^*\pi^\pm(X)$ and $\mathrm{B}_J^* \to \mathrm{B}\pi^\pm(X)$ decays. Figures 9 and 10 show the $\mathrm{B}\pi^\pm$ mass distributions for the B^*-enriched and the B^*-depleted sample, respectively. The Monte Carlo background distributions of both samples are corrected using a procedure explained in Sections 6 and 8 and the same fit as for the background of the total B_J^* sample (see Section 6) is performed. The fitted background functions are normalised in the sideband region $6.10 \ \mathrm{GeV}/c^2 < M_{\mathrm{B}\pi} < 7.10 \ \mathrm{GeV}/c^2$ and subtracted from the corresponding data distributions. From the resulting signal peaks, $\mathrm{BR}(\mathrm{B}_J^* \to \mathrm{B}^*\pi(X))$ is obtained. Assuming that B_J^* decay to B^* or B only and with the efficiency ratios defined as above, we derive the following formula:

$$
\begin{aligned}
\mathrm{BR}(\mathrm{B}_J^* \to \mathrm{B}^*\pi(X)) &= \frac{\mathrm{BR}(\mathrm{B}_J^* \to \mathrm{B}^*\pi(X))}{\mathrm{BR}(\mathrm{B}_J^* \to \mathrm{B}^*\pi(X)) + \mathrm{BR}(\mathrm{B}_J^* \to \mathrm{B}\pi(X))} \\
&= e_0 \cdot \frac{N_{\mathrm{E}} - e \cdot N_{\mathrm{D}}}{(e_0 - e^*) \cdot N_{\mathrm{E}} + (1 - e \cdot e_0) \cdot N_{\mathrm{D}}} \quad ,
\end{aligned} \tag{8}
$$

where N_{E} (N_{D}) denotes the number of B_J^* signal entries of the B^*-enriched (B^*-depleted) sample. In the data, $N_{\mathrm{E}} = (8782 \pm 252_{\mathrm{stat}})$ and $N_{\mathrm{D}} = (12051 \pm 295_{\mathrm{stat}})$ B_J^* candidates are observed in the $M_{\mathrm{B}\pi}$ signal window $(5.3 - 6.1) \ \mathrm{GeV}/c^2$. Using the numbers for the efficiency ratios e_0, e and e^* presented in Table 2, we calculate $\mathrm{BR}(\mathrm{B}_J^* \to \mathrm{B}^*\pi(X)) = 0.85$.

The statistical errors on N_{E} and N_{D} result in a total error on the branching ratio of ± 0.13. Besides this error, statistical uncertainties due to the sideband normalisation have been taken into account. Since the samples are mutually exclusive, the statistical errors of the sideband normalisation of both samples are independent. The contributions of the B^*-enriched and the B^*-depleted sample sideband normalisation to the statistical error on $\mathrm{BR}(\mathrm{B}_J^* \to \mathrm{B}^*\pi(X))$ are $^{+0.17}_{-0.18}$ and ± 0.15, respectively. Adding all quoted errors in quadrature, the branching ratio of orbitally-excited B mesons decaying into B^* is measured to be

$$
\mathrm{BR}(\mathrm{B}_J^* \to \mathrm{B}^*\pi(X)) = 0.85 \, ^{+0.26}_{-0.27} \quad ,
$$

where the error is statistical only. This branching ratio includes all decays of the type $\mathrm{B}_J^* \to \mathrm{B}^{(*)}\pi X$, as no cut against additional B_J^* decay products is applied. Consequently, the notation

$BR(B_J^* \to B^*\pi(X))$ is chosen. Systematic uncertainties, especially of the efficiency ratios and the combinatorial $B\pi$ background are discussed in Section 8.

We further investigate the composition of the B_J^* sample by splitting the sample into $B_J^* \to B^*\pi^\pm(X)$ and $B_J^* \to B\pi^\pm(X)$ components. By subtracting from the $B\pi$ mass distribution of the B^*-enriched sample the corresponding distribution of the B^*-depleted sample multiplied by a scale factor, a $B\pi^\pm$ mass distribution containing $B_J^* \to B^*\pi^\pm(X)$ transitions only is obtained. The scale factor is the ratio of the $B_J^* \to B\pi^\pm$ efficiencies of both samples, $e = \varepsilon_\mathrm{E}/\varepsilon_\mathrm{D}$. In a similar way, a mass distribution with $B_J^* \to B^*\pi^\pm(X)$ decays subtracted off is obtained. The corresponding efficiency-corrected $B\pi^\pm$ mass distributions for pure $B_J^* \to B^*\pi^\pm(X)$ and pure $B_J^* \to B\pi^\pm(X)$ transitions are shown in Figure 11. The number of signal entries in the $B\pi^\pm$ mass distributions of Figures 11a and 11b depends on the ratio $BR(B_J^* \to B^*\pi(X))$ as well as on the efficiency ratios defined in Table 2.

A significant excess of entries is seen in the pure $B_J^* \to B^*\pi^\pm(X)$ distribution at masses around 5.7 GeV/c^2 with tails down to 5.5 GeV/c^2 and up to 6.0 GeV/c^2. The narrow peak in the $B_J^* \to B^*\pi^\pm(X)$ distribution is most likely due to $B_1(3/2) \to B^*\pi^\pm$ and $B_2^* \to B^*\pi^\pm$ decays. To obtain the true mass values of the $B^*\pi$ states, the entries have to be shifted to higher masses by 46 MeV/c^2.

In the pure $B_J^* \to B\pi^\pm(X)$ mass distribution, a small excess is observed in the region up to 5.85 GeV/c^2. This excess can be assigned to the decays $B_2^* \to B\pi^\pm$ and $B_0^* \to B\pi^\pm$. Since the statistical significance of the excess in the $B_J^* \to B\pi^\pm(X)$ mass distribution is small, no further conclusion is drawn from Figure 11b.

7.2 Simultaneous fit to the $B\pi^\pm$ mass spectra

A simultaneous fit is performed to the background subtracted and efficiency corrected $B\pi$ mass spectra shown in Figures 9c and 10c. Several assumptions are made on the nature of the observed signal to reduce the number of free fit parameters:

- The signal excess stems from B_J^* decays only. Contributions from B_{sJ}^* decays, $B^{(*)\prime} \to B^{(*)}\pi$ and $B^{(*)\prime} \to B^{(*)}\pi\pi$ do not exceed a few percent [5, 10, 33] and are therefore not implemented in the fit but considered as sources of systematic uncertainties. Any other excited state eventually contributing to the signal peak is ignored since there is no experimental evidence for such states and theoretical predictions give negligible production rates.

- The heavy quark limit $m_Q \to \infty$ holds to describe the four B_J^* states. Therefore, according to spin-parity conservation, one expects five different mass peaks from single pion transitions as listed in the first paragraph of Section 1 and shown in Figure 1. Furthermore, the physical B_1 states are $B_1(1/2)$ and $B_1(3/2)$ and thus no mixing occurs.

- Partners of the same doublet are assumed to have similar properties. The constraints on masses, widths and production rates used in the fit are presented in Table 3. The mass splitting between the narrow states can be calculated using the corresponding mass splitting of the D_J^* which has been measured [2]. The mass splitting between the broad states is expected to be of about the same size. Also the order of magnitude of the widths of the narrow and broad B_J^* states can be estimated from experimental D_J^* results [2, 34].

- Only the decay modes listed in Table 3 are taken into account. We explicitly allow the decay via two pions to B^* and B for all B_J^* states. For each B_J^* state, we set $BR(B_J^* \to$

state	J_j^P	fit constraints			allowed decay modes
		production rate	mass	width	
B_0^*	$0_{1/2}^+$	$f(b \to B_0^*)$	free	free	$B\pi$, $B^*\pi\pi$, $B\pi\pi$
$B_1(\frac{1}{2})$	$1_{1/2}^+$	$f(b \to B_0^*)$	$M(B_0^*) + 20$ MeV/c^2	$1.25 \cdot \Gamma(B_0^*)$	$B^*\pi$, $B^*\pi\pi$, $B\pi\pi$
$B_1(\frac{3}{2})$	$1_{3/2}^+$	$\frac{3}{2} \cdot f(b \to B_0^*)$	free	free	$B^*\pi$, $B^*\pi\pi$, $B\pi\pi$
B_2^*	$2_{3/2}^+$	$\frac{3}{2} \cdot f(b \to B_0^*)$	$M(B_1(\frac{3}{2})) + 12$ MeV/c^2	$1.00 \cdot \Gamma(B_1(\frac{3}{2}))$	$B^*\pi$, $B\pi$, $B^*\pi\pi$, $B\pi\pi$

Table 3: Constraints on production rates, masses and widths used in the fit to the total $B\pi$ mass spectrum.

$B^*\pi\pi) = BR(B_J^* \to B\pi\pi)$ and we assume the same branching ratio $BR(B_J^* \to B^{(*)}\pi\pi)$ for all B_J^* states. For the B_2^*, we set $BR(B_2^* \to B^*\pi) = BR(B_2^* \to B\pi)$.

- The fraction of narrow states $f_{narrow} = (f(b \to B_1(3/2)) + f(b \to B_2^*))/f(b \to B_J^*)$ is fixed to 0.6. This number is the average of $1/2$, $2/3$ and $2/3$ corresponding to production rates of narrow B_J^* according to state counting, total spin counting and light quark spin counting, respectively. To justify this constraint, a fit to the total $B\pi$ mass spectrum is performed with f_{narrow} as an additional free parameter.

- The mass splitting between B and B^* is fixed to the current world average [2].

- Each of the five single pion decay modes is represented by a Breit-Wigner function convoluted with the $M_{B\pi}$ dependent resolution function explained in Section 6.2 and shown in Figure 8. To take into account the phase-space suppression at threshold, asymmetric Breit-Wigner functions with the threshold factor [35]

$$f_{threshold}(M) = \sqrt{\left(1 - \frac{M_B^2}{M^2} - \frac{M_\pi^2}{M^2}\right)^2 - 4 \cdot \frac{M_B^2 M_\pi^2}{M^4}} \qquad (9)$$

are used instead of the symmetric Breit-Wigner functions for the broad states.

- For the di-pion transitions, the signal shape including the detector resolution is taken from simulated $B_J^* \to B^{(*)}\pi\pi$ decays. Simple Gaussians truncated at threshold give a good description of the simulated satellite peaks. The mean of the Gaussian depends linearly on the mass difference between B_J^* and B ground state. The width of the Gaussian is also a function of this mass splitting and depends on the width of the B_J^* state. The functions to parameterise the mean and width of the Gaussians are taken from the simulation. No attempt is made to implement different signal shapes for decays where the two pions form an intermediate resonance or for cascade transitions from high mass B_J^* states via low mass B_J^* states to the ground states B^* and B [13].

The different reconstruction efficiencies for $B_J^* \to B^*\pi^\pm$ and $B_J^* \to B\pi^\pm$ decays of the B^*-enriched and B^*-depleted signals are taken from Monte Carlo (see Table 2). As the specific peaks that make up the total B_J^* signal have different sizes in the B^*-enriched and B^*-depleted

---

[13] Strong decays within the B_J^* multiplet are allowed if the mass splitting within the multiplet or some of the widths are larger than the pion mass.

mass distributions, different enhancements or depletions are expected for specific regions of the $B\pi^\pm$ mass spectra according to the assumptions on the nature of the B_J^* signal. Thus the simultaneous fit provides a non-trivial consistency check of the $BR(B_J^* \to B^*\pi(X))$ result of Section 7.1 and of some of the constraints used in the fit.

The implementation of $BR(B_J^* \to B^*\pi)$ as a fit parameter causes some complications. Note that the $BR(B_J^* \to B^*\pi(X))$ result of Section 7.1 includes transitions of narrow B_J^* and broad B_J^* via emission of one pion (and perhaps other decay products). The branching fraction to the B^* ground state might be different for narrow and broad states and also different for $B^*\pi$ and $B^*\pi\pi$ final states. Whereas the result obtained from Equation 8 is the average of the natural composition of the different decay modes, four different parameters have to be considered for this fit: $BR(B_{J\text{narrow}}^* \to B^*\pi)$, $BR(B_{J\text{broad}}^* \to B^*\pi)$, $BR(B_{J\text{narrow}}^* \to B^*\pi\pi)$ and $BR(B_{J\text{broad}}^* \to B^*\pi\pi)$. Monte Carlo studies indicate that the sensitivity of the fit to $BR(B_{J\text{narrow}}^* \to B^*\pi\pi)$ and $BR(B_{J\text{broad}}^* \to B^*\pi\pi)$ is negligible since shape and position of the corresponding peaks in the $B\pi^\pm$ mass spectra are almost the same for the $B^*\pi\pi$ and $B\pi\pi$ final states. The sensitivity to $BR(B_{J\text{broad}}^* \to B^*\pi)$ is also smaller than the corresponding sensitivity to $BR(B_{J\text{narrow}}^* \to B^*\pi)$ since a large width but a comparable intra-doublet mass splitting of the B_J^* states makes a separation of the decay modes of broad B_J^* to $B^*\pi$ and $B\pi$ difficult. To reduce the number of fit parameters and to keep the correlations between the fit parameters small, $BR(B_{J\text{narrow}}^* \to B^*\pi\pi)/(BR(B_{J\text{narrow}}^* \to B^*\pi\pi) + BR(B_{J\text{narrow}}^* \to B\pi\pi))$ and $BR(B_{J\text{broad}}^* \to B^*\pi\pi)/(BR(B_{J\text{broad}}^* \to B^*\pi\pi) + BR(B_{J\text{broad}}^* \to B\pi\pi))$ are fixed to 0.5 in the fit. Furthermore, we require $BR(B_{J\text{narrow}}^* \to B^*\pi) = \frac{3}{2} \cdot BR(B_{J\text{broad}}^* \to B^*\pi)$ and the fit parameter $BR(B_J^* \to B^*\pi)$ is the weighted mean of both numbers according to the production rates of broad and narrow B_J^*. The factor $\frac{3}{2}$ is based on the assumption of the same production rates for states within the same doublet and $BR(B_2^* \to B^*\pi)/(BR(B_2^* \to B^*\pi) + BR(B_2^* \to B\pi)) = 0.5$. The fit constraints explained in this paragraph are listed in Table 4.

fit constraint	value
$\dfrac{BR(B_{J\text{narrow}}^* \to B^*\pi\pi)}{(BR(B_{J\text{narrow}}^* \to B^*\pi\pi) + BR(B_{J\text{narrow}}^* \to B\pi\pi))}$	$\frac{1}{2}$
$\dfrac{BR(B_{J\text{broad}}^* \to B^*\pi\pi)}{(BR(B_{J\text{broad}}^* \to B^*\pi\pi) + BR(B_{J\text{broad}}^* \to B\pi\pi))}$	$\frac{1}{2}$
$\dfrac{BR(B_{J\text{narrow}}^* \to B^*\pi)}{BR(B_{J\text{broad}}^* \to B^*\pi)}$	$\frac{3}{2}$

Table 4: Additional fit constraints used in the simultaneous fit.

With the constraints discussed above (see also Tables 3 and 4) the remaining free parameters are: sum of the number of entries of the B^*-enriched and the B^*-depleted signal, $M(B_1(3/2))$, $\Gamma(B_1(3/2))$, $M(B_0^*)$, $\Gamma(B_0^*)$, $BR(B_J^* \to B^{(*)}\pi\pi)$ and $BR(B_J^* \to B^*\pi)$. A fit [36] is performed to the simulated B_J^* signals using the full Monte Carlo statistics. All fit results lie within 1σ of the Monte Carlo input value. We fit the $B\pi^\pm$ mass spectra of Figures 9c and 10c simultaneously. The least squares fit is performed in the $B\pi$ mass region of $5.40 - 6.10$ GeV/c^2 with a bin width of 20 MeV/c^2. The fit results are

$$M(B_1(3/2)) = (5.738^{+0.005}_{-0.006}) \text{ GeV}/c^2$$
$$\Gamma(B_1(3/2)) = (18^{+15}_{-13}) \text{ MeV}/c^2$$

$$M(\mathrm{B}_0^*) = (5.839 \,{}^{+\,0.013}_{-\,0.014}) \,\mathrm{GeV}/c^2 \qquad (\star)$$
$$\Gamma(\mathrm{B}_0^*) = (129 \,{}^{+\,27}_{-\,23}) \,\mathrm{MeV}/c^2 \qquad (\star)$$
$$\mathrm{BR}(\mathrm{B}_J^* \to \mathrm{B}^{(*)}\pi\pi) = 0.245 \,{}^{+\,0.027}_{-\,0.028} \qquad (\star)$$
$$\mathrm{BR}(\mathrm{B}_J^* \to \mathrm{B}^*\pi) = 0.74 \,{}^{+\,0.12}_{-\,0.10}$$

where the errors are of statistical origin only. The fit probability is 65% and the result is presented in Figures 12 and 13. The fit results are in agreement with the interpretation of the B_J^* signals of Figure 11 given in Section 7.1. Numbers labelled with $(\star)$ should be taken with care because of large systematic errors. The robustness of the fit results will be discussed in Section 8.

Note that the statistical error of the $\mathrm{BR}(\mathrm{B}_J^* \to \mathrm{B}^*\pi(X))$ measurement presented in Section 7.1 includes the errors arising from the sideband normalisation. The statistical errors of the fit results on the other hand do not include the sideband normalisation errors. The latter will be discussed in Section 8. The $\mathrm{BR}(\mathrm{B}_J^* \to \mathrm{B}^*\pi)$ result of the fit does not include decays to B^* via di-pion emission. The $\mathrm{BR}(\mathrm{B}_J^* \to \mathrm{B}^{(*)}\pi\pi)$ result is corrected by a factor of 0.75 to account for double counting of the $\mathrm{B}^{(*)}\pi^+\pi^-$ final state. In Table 5 the correlations between all fit parameters are shown. Systematic uncertainties of the fit results are discussed in detail in Section 8.

parameter	$N(\mathrm{B}_J^*)$	$M(\mathrm{B}_1)$	$\Gamma(\mathrm{B}_1)$	$M(\mathrm{B}_0^*)$	$\Gamma(\mathrm{B}_0^*)$	$\mathrm{BR}(\mathrm{B}_J^* \to \mathrm{B}^{(*)}\pi\pi)$	$\mathrm{BR}(\mathrm{B}_J^* \to \mathrm{B}^*\pi)$
$N(\mathrm{B}_J^*)$	1.000	0.078	0.349	-0.108	0.418	-0.088	0.114
$M(\mathrm{B}_1(3/2))$	0.078	1.000	0.394	0.028	-0.032	0.067	0.731
$\Gamma(\mathrm{B}_1(3/2))$	0.349	0.394	1.000	-0.675	0.355	-0.764	0.791
$M(\mathrm{B}_0^*)$	-0.108	0.028	-0.675	1.000	-0.313	0.741	-0.380
$\Gamma(\mathrm{B}_0^*)$	0.418	-0.032	0.355	-0.313	1.000	-0.473	-0.036
$\mathrm{BR}(\mathrm{B}_J^* \to \mathrm{B}^{(*)}\pi\pi)$	-0.088	0.067	-0.764	0.741	-0.473	1.000	-0.437
$\mathrm{BR}(\mathrm{B}_J^* \to \mathrm{B}^*\pi)$	0.114	0.731	0.791	-0.380	-0.036	-0.437	1.000

Table 5: Table of correlations of all free parameters in the final fit to the data mass spectra of the B^*-enriched and B^*-depleted samples.

8 Systematic uncertainties

In the following sections, the determination of the systematic uncertainties is presented separately for the model-independent $\mathrm{BR}(\mathrm{B}_J^* \to \mathrm{B}^*\pi(X))$ measurement and for the results obtained from the simultaneous fit to the $\mathrm{B}\pi^\pm$ mass spectra with different B^* content.

8.1 Systematic error on the $\mathrm{BR}(\mathrm{B}_J^* \to \mathrm{B}^*\pi(X))$ measurement

For the $\mathrm{BR}(\mathrm{B}_J^* \to \mathrm{B}^*\pi(X))$ measurement, the dominant sources of systematic error are uncertainties in the efficiency ratios, the modelling of the combinatorial $\mathrm{B}\pi^\pm$ background and systematic errors on the sideband normalisation of the B^*-enriched and B^*-depleted samples. Each contribution to the total error on $\mathrm{BR}(\mathrm{B}_J^* \to \mathrm{B}^*\pi(X))$ is listed in Table 6.

8.1.1 Reconstruction efficiencies

Monte Carlo simulations are used to calculate the efficiency ratios e, e^* and e_0. The systematic errors on these ratios are dominated by uncertainties in the photon reconstruction. The simulation is checked against data using known properties of B* and π^0. The latter are formed by a pairwise combination of two good conversion candidates or one good conversion and one good calorimeter candidate assigned to the same B candidate.

- We perform direct checks of the photon reconstruction efficiencies: The yields of the Monte Carlo B* and π^0 mass peaks are consistent with the results observed in data with the simulated B* and π^0 production rates being in agreement with earlier measurements [2]. To account for the statistical error of the number of B* and π^0 peak entries and for possible uncertainties in the simulated production rates, the calculation of efficiency ratios is repeated on Monte Carlo with the reconstruction efficiency of conversion (calorimeter) photons in the decay B* → Bγ changed by $\pm 10\%$ ($^{+15}_{-10}\%$). The variation of $+15\%$ reflects a small discrepancy observed in the simulated and measured B* yields of the calorimeter sample.

- In a B$_J^*$ decay, the helicity angle θ^* is the angle between the signal pion momentum measured in the B$_J^*$ rest frame and the momentum of the B$_J^*$ in the lab frame. As the signal pion selection acceptance depends on $\cos\theta^*$, the B$_J^*$ efficiency is sensitive to the shape of $\cos\theta^*$. The distributions of helicity angle for B$_0^*$ and B$_1(1/2)$ decays are assumed to be flat (S-wave transitions) and according to [37] the B$_1(3/2)$ and the B$_2^*$ are expected to have the same $\cos\theta^*$ distribution for any initial b polarisation:

$$\frac{1}{\Gamma}\frac{\mathrm{d}\Gamma}{\mathrm{d}\cos\theta^*}(\mathrm{B}_1(3/2), \mathrm{B}_2^* \to \mathrm{B}, \mathrm{B}^*\pi) = \frac{1}{4}\left(1 + 3\cos^2\theta^* - 6w_{3/2}(\cos^2\theta^* - \frac{1}{3})\right) \qquad (10)$$

where $w_{3/2}$ is the probability that fragmentation leads to a state with the maximum helicity value of $3/2$ for the light degrees of freedom. The Monte Carlo $\cos\theta^*$ distributions of B$_1(3/2)$ and B$_2^*$ have been reweighted to cover the whole range $w_{3/2} = 0 - 1$.

- The number of good calorimeter photon candidates $N_{\gamma_{\mathrm{ECAL}}}$ (Figure 3b) is not modelled well in the simulation. Therefore, the Monte Carlo distribution is reweighted to the corresponding data distribution. The reweighting clearly improves the general agreement between data and Monte Carlo and has an impact on the efficiency rations e, e^* and e_0. The central value of $\mathrm{BR}(\mathrm{B}_J^* \to \mathrm{B}^*\pi(X))$ changes by -0.059 due to the reweighting. To quantify the uncertainty in the reweighting procedure we take half of the total change of the central value as the error on $\mathrm{BR}(\mathrm{B}_J^* \to \mathrm{B}^*\pi(X))$.

- The mass dependent efficiency correction to the B$_J^*$ signal for both the B*-enriched and B*-depleted samples produces a deviation in $\mathrm{BR}(\mathrm{B}_J^* \to \mathrm{B}^*\pi(X))$ relative to the result without mass dependent efficiency correction. To account for any mismodelling in the simulated B$_J^*$ masses and the simulated mass dependence of the efficiency, half of this deviation is taken as the systematic error.

- The calculated efficiency ratios are uncertain due to limited Monte Carlo statistics.

- We check the calibration of the photon energy measurement by comparing the measured and simulated shapes and peak positions of both the B* and the π^0. There is agreement within the statistical errors. This results in small (negligible) errors on the efficiencies of the calorimeter (conversion) sample.

8.1.2   Background related uncertainties

Uncertainties in the shape of the simulated background have an impact on the number of signal candidates $N_{\rm E}$ and $N_{\rm D}$. Since the combinatorial backgrounds in both the B*-enriched and the B*-depleted samples are affected by systematic shifts in a similar way, the measurement is rather robust against possible uncertainties in the Monte Carlo background simulation. For the determination of systematic errors, the simulated Bπ background is varied using the methods described below. For each variation, the Monte Carlo background is normalised and subtracted from the data and the number of signal entries N_E and N_D are counted.

- Data test samples are developed in which individual background sources are substantially enhanced to study the B$\pi^\pm$ combinatorial background. The background is divided into three different classes: tracks combined with mistagged B candidates in light and charm quark events (udsc flavour), b hadron decay tracks combined with true b hadrons (b hadron decay) and b fragmentation tracks combined with true b hadrons (b fragmentation). The selection criteria for each test sample are chosen to cover a large fraction of the kinematic region of the signal pion selection. A purity of at least 90% for the background source under study and a B$_J^*$ signal fraction smaller than 1.5% is obtained by inverting cuts in the original B$_J^*$ selection. For the light and charm quark background, also a sample of D^{*+} candidates reconstructed as described in [38] is used as a qualitative cross check. For each test sample, the B$\pi^\pm$ invariant mass distribution observed in data is compared with the Monte Carlo distribution normalised to the same number of selected B candidates. The mass distributions and their bin-by-bin ratios data/Monte Carlo are shown in Figure 14. The different ratios are fitted with simple polynomials. The latter are used to correct the shape of the original Monte Carlo B$\pi^\pm$ mass distributions for each background source separately. The systematic uncertainty on each background source is given by the difference in BR(B$_J^* \to$ B$^*\pi(X)$) between using the corrected and the uncorrected shape of the B$\pi^\pm$ mass distribution.

- The composition of the B$\pi^\pm$ background, as seen in the Monte Carlo after the corrections have been applied, is varied for each source. The fraction of each of the three background sources described earlier is varied by $\pm 20\%$.

- The Peterson fragmentation parameter $\epsilon_{\rm b}$ has been varied in the range $0.0028 - 0.0057$ to cover uncertainties in the average fraction of the beam energy carried by the weakly decaying b hadron, $\langle x_E \rangle$, and in the shape of the fragmentation function. This variation causes a minor change in the B$\pi^\pm$ background shape. The effect on BR(B$_J^* \to$ B$^*\pi(X)$) is smaller than 0.002.

- The average charged multiplicity of weakly decaying b hadrons (including K^0 and Λ decay products) is varied in the range $5.375 - 5.865$ in the simulation (see [39]). The observed effect on the B$\pi^\pm$ background shape results in a negligible change of BR(B$_J^* \to$ B$^*\pi(X)$).

8.1.3   Other sources of systematic uncertainties and consistency checks

The following systematic studies have been performed in addition to the studies described in Sections 8.1.1 and 8.1.2.

- The range of the sideband used for the background normalisation is varied by ± 100 MeV/c^2 on each side for both the B*-enriched and B*-depleted sample. This variation is motivated

source	range	$\Delta(\mathrm{BR}(\mathrm{B}_J^* \to \mathrm{B}^*\pi(X)))$
B* efficiency (ECAL) variation	$[0.90, 1.15]$	$+0.036 \ -0.047$
B* efficiency ($\gamma \to \mathrm{e}^+\mathrm{e}^-$) variation	$[0.90, 1.10]$	$+0.019 \ -0.018$
$\cos\theta^*$ dependency	$w_{3/2} \in [0,1]$	$+0.040 \ -0.034$
reweighting of $N_{\gamma_{\mathrm{ECAL}}}$		± 0.030
$M_{\mathrm{B}\pi}$ dependence of B_J^* efficiency		± 0.018
statistical error on efficiency ratios	$\approx 1\%$	± 0.018
reconstructed B* mass (ECAL)	$\pm 2\,\mathrm{MeV}/c^2$	$+0.007 \ -0.005$
relative composition of background sources	$\pm 20\%$	$+0.027 \ -0.037$
B decay tracks background modelling	corr. on/off	± 0.017
b fragmentation tracks background modelling	corr. on/off	± 0.005
udsc tracks background modelling	corr. on/off	± 0.002
sideband range variation	$\pm 100\,\mathrm{MeV}/c^2$	$+0.076 \ -0.057$
variation of cuts on $\mathcal{W}(\mathrm{B}^*)$		$+0.030 \ -0.043$
B_{sJ}^* reflections		$+0.006 \ -0.026$
$\mathrm{B}^{(*)\prime}$ reflections		$+0.000 \ -0.017$
track parameter resolution variation	$\pm 10\%$	< 0.010
total		$+0.12 \ -0.12$

Table 6: Systematic errors of the $\mathrm{BR}(\mathrm{B}_J^* \to \mathrm{B}^*\pi(X))$ measurement. Detailed information for each uncertainty is given in the text, as well as a discussion of uncertainties which are negligible and thus excluded from this table.

by the range and shape of the B_J^* signal observed in Figure 7. The quadratic sum of the differences observed in the number of signal entries gives the largest error contribution to the systematic error of the $\mathrm{BR}(\mathrm{B}_J^* \to \mathrm{B}^*\pi(X))$ measurement.

- The cut on $\mathcal{W}(\mathrm{B}^*)$ has been varied. All cut values producing a ratio of signal to noise ratios of the B*-enriched and B*-depleted samples between 0.9 and 1.1 are considered. The observed deviations in $\mathrm{BR}(\mathrm{B}_J^* \to \mathrm{B}^*\pi(X))$ do not exceed $^{+0.030}_{-0.043}$ which is taken as the systematic error.

- The amount of B_{sJ}^* seen in the B_J^* peaks is less than 4% for a B_{sJ}^* production rate consistent with [5]. The branching ratio $\mathrm{BR}(\mathrm{B}_{sJ}^* \to \mathrm{B}^*\mathrm{K})$ is varied from 0.2 to 1.0 in the simulation.

- Contributions from radial excitations of B mesons decaying to $\mathrm{B}^{(*)}\pi$ or $\mathrm{B}^{(*)}\pi\pi$ may be present in the B_J^* signal [10, 33]. Monte Carlo studies with simulated $\mathrm{B}' \to \mathrm{B}\pi^+\pi^-$ and $\mathrm{B}^{*\prime} \to \mathrm{B}^*\pi^+\pi^-$ decays[14] indicate a contamination of the B_J^* signal around $M_{\mathrm{B}\pi} = 5.6\,\mathrm{GeV}/c^2$. With the total $\mathrm{B}^{(*)\prime}$ production rate observed in [33], the B_J^* peak of Figure 7 does not contain more than 3% $\mathrm{B}^{(*)\prime}$ transitions. The fraction of B' in the simulated $\mathrm{B}^{(*)\prime}$ sample is varied from 0.3 to 0.7.

- To account for any uncertainties arising from a wrongly simulated tracking resolution, the reconstructed track parameters are smeared by $\pm 10\%$ in the Monte Carlo [28].

- The cuts of the signal pion selection have been varied. No systematic deviations are observed.

---
[14]using $M(\mathrm{B}') = 5.883\,\mathrm{GeV}/c^2$ and $M(\mathrm{B}^{*\prime}) = 5.898\,\mathrm{GeV}/c^2$ according to [11] and in agreement with [33]

- The whole analysis is repeated using conversion photons only and calorimeter photons only. The obtained $\mathrm{BR}(\mathrm{B}^*_J \to \mathrm{B}^*\pi(X))$ results and the $\mathrm{B}^*_J \to \mathrm{B}^*\pi^\pm(X)$ and $\mathrm{B}^*_J \to \mathrm{B}\pi^\pm(X)$ mass distributions are in agreement with each other and with the total sample.

- Varying the cut on $\mathcal{B}_{\mathrm{event}}$ so that the b purity changes from 92% to 98% produces no systematic deviation in $\mathrm{BR}(\mathrm{B}^*_J \to \mathrm{B}^*\pi(X))$.

- A neural network has been trained to replace the weight $\mathcal{W}(\mathrm{B}^*)$ obtained from the Monte Carlo purity parameterisation. The neural network output is strongly correlated with the weight $\mathcal{W}(\mathrm{B}^*)$ and does not improve the B^*/B separation.

All systematic errors considered for $\mathrm{BR}(\mathrm{B}^*_J \to \mathrm{B}^*\pi(X))$ are added up in quadrature, resulting in a total error on $\mathrm{BR}(\mathrm{B}^*_J \to \mathrm{B}^*\pi(X))$ of ± 0.12 (see Table 6).

8.2 Systematic uncertainties on the results of the simultaneous fit to the B*-enriched and B*-depleted mass spectra

All sources of systematic error are varied in turn within the estimated uncertainty range and the fit presented in Section 7.2 is repeated. If not stated otherwise, the observed deviation with respect to the original fit is taken as a systematic error for each fit parameter. The total systematic error on each fit parameter is the quadratic sum of all individual error contributions. This procedure takes into account the correlations between the fit parameters. All systematic uncertainties are listed in Table 7.

8.2.1 Variation of fit constraints

The fit constraints are varied according to the present knowledge of D^*_J properties [2] and theoretical considerations [3, 4, 11–14]:

- $\mathrm{BR}(\mathrm{B}^*_{J\,\mathrm{broad}} \to \mathrm{B}^*\pi)$ was fixed to $\frac{2}{3} \cdot \mathrm{BR}(\mathrm{B}^*_{J\,\mathrm{narrow}} \to \mathrm{B}^*\pi)$. This constraint is changed to $\mathrm{BR}(\mathrm{B}^*_{J\,\mathrm{broad}} \to \mathrm{B}^*\pi) = \mathrm{BR}(\mathrm{B}^*_{J\,\mathrm{narrow}} \to \mathrm{B}^*\pi)$ and the corresponding deviations of the fit parameters are taken as systematic errors.

- The ratio of the widths of partners of the same doublet was fixed to $\Gamma(\mathrm{B}^*_2)/\Gamma(\mathrm{B}_1(3/2)) = 1.25$ and $\Gamma(\mathrm{B}_1(1/2))/\Gamma(\mathrm{B}^*_0) = 1.00$. We allow a variation of the ratio of widths of 1.0-1.4 for the narrow states and 0.7-1.4 for the broad states.

- The relative production rates $\mathrm{f}(\mathrm{b} \to \mathrm{B}^*_0) : \mathrm{f}(\mathrm{b} \to \mathrm{B}_1(1/2)) : \mathrm{f}(\mathrm{b} \to \mathrm{B}_1(3/2)) : \mathrm{f}(\mathrm{b} \to \mathrm{B}^*_2)$ were fixed to $2 : 2 : 3 : 3$. We vary the production rate ratio $\mathrm{f}(\mathrm{b} \to \mathrm{B}_1(3/2))/(\mathrm{f}(\mathrm{b} \to \mathrm{B}_1(3/2))+\mathrm{f}(\mathrm{b} \to \mathrm{B}^*_2))$ in the range 0.375-0.600, $\mathrm{f}(\mathrm{b} \to \mathrm{B}^*_0)/(\mathrm{f}(\mathrm{b} \to \mathrm{B}^*_0)+\mathrm{f}(\mathrm{b} \to \mathrm{B}_1(1/2)))$ in the range 0.250-0.600 and $\mathrm{f}_{\mathrm{narrow}}$ in the range 0.5-0.75. These variations cover the different production rate estimates of state counting (1:1:1:1) to total spin counting (1:3:3:5).

- The constraint $\mathrm{BR}(\mathrm{B}^*_2 \to \mathrm{B}^*\pi) = \mathrm{BR}(\mathrm{B}^*_2 \to \mathrm{B}\pi)$ was used. We allow a variation of $\mathrm{BR}(\mathrm{B}^*_2 \to \mathrm{B}^*\pi)/(\mathrm{BR}(\mathrm{B}^*_2 \to \mathrm{B}^*\pi) + \mathrm{BR}(\mathrm{B}^*_2 \to \mathrm{B}\pi)) = 0.3 - 0.7$.

- Whereas the mass splitting between the $j_q = 1/2$ and $j_q = 3/2$ doublets was free in the fit, the mass splittings within the doublets were fixed. We allow a variation of $M(\mathrm{B}^*_2) - M(\mathrm{B}_1(3/2)) = (5 - 20)$ MeV/c^2 and $M(\mathrm{B}_1(1/2)) - M(\mathrm{B}^*_0) = (0 - 50)$ MeV/c^2.

- The ratio $\mathrm{BR}(\mathrm{B}_J^* \to \mathrm{B}^*\pi\pi)/(\mathrm{BR}(\mathrm{B}_J^* \to \mathrm{B}^*\pi\pi) + \mathrm{BR}(\mathrm{B}_J^* \to \mathrm{B}\pi\pi))$, which was fixed to 0.5, is varied in the range 0.3-0.7. No significant deviation in the fit parameters is observed, since the position and shape of the peaks corresponding to the two final states are very similar.

8.2.2   Reconstruction efficiencies

The B_J^* reconstruction efficiency is a function of the reconstructed $\mathrm{B}\pi$ mass and the angular distribution of the π. The efficiency is taken from the Monte Carlo and possible problems with its simulation are taken into account:

- The signal pion selection cuts have been varied. Whereas the Monte Carlo simulation describes the reconstruction efficiency well at high $\mathrm{B}\pi$ masses, this statement can not be proven for low $\mathrm{B}\pi$ masses. Therefore, we perform the fit to the B_J^* signal without an acceptance correction of the mass spectrum as shown in Figure 7b. Although the fit result has a low fit probability, we assign half of the total deviations of the fit parameters observed with respect to the original fit as systematic errors. This results in a large systematic error on $\mathrm{BR}(\mathrm{B}_J^* \to \mathrm{B}^{(*)}\pi\pi)$.

- Systematic uncertainties arising from the photon reconstruction as well as from the unknown $\cos\theta^*$ distributions are determined using the methods presented in 8.1.1.

8.2.3   Background related uncertainties

- The uncertainties due to the limited data statistics in the upper sideband regions of the B^*-enriched and B^*-depleted samples produce quite large error contributions on $\mathrm{BR}(\mathrm{B}_J^* \to \mathrm{B}^*\pi)$. For the fit results, these error contributions are treated as systematic errors and have to be compared with the corresponding errors obtained for the model-independent $\mathrm{BR}(\mathrm{B}_J^* \to \mathrm{B}^*\pi(X))$ measurement. While the sideband range used for the background normalisation is the same for both measurements, the error of the $\mathrm{BR}(\mathrm{B}_J^* \to \mathrm{B}^*\pi)$ fit result is smaller because the fit makes explicit use of the shape and of the composition of the B_J^* mass distributions.

- The Peterson fragmentation parameter ϵ_b and the charged particle multiplicity of weakly decaying b hadrons are varied in the simulation as described in Section 8.1.2. The multiplicity variation has no effect on the fit results.

- To evaluate the uncertainty due to the function used to fit the Monte Carlo background, we directly subtract the corrected Monte Carlo background histograms of the $\mathrm{B}\pi$ mass distributions from the corresponding data histograms.

- The range of the sideband used for the background normalisation is varied by ± 100 MeV/c^2 on each side and the observed deviations are added in quadrature.

- For the determination of the shape and the composition of the $\mathrm{B}\pi$ background, the same methods as presented in Section 8.1.2 are used.

source	$\Delta\mathrm{BR}$ $(\mathrm{B}_J^* \to \mathrm{B}^*\pi)$	$\Delta M(\mathrm{B}_1(\frac{3}{2}))$	$\Delta\Gamma(\mathrm{B}_1(\frac{3}{2}))$	$\Delta M(\mathrm{B}_0^*)$	$\Delta\Gamma(\mathrm{B}_0^*)$	$\frac{1}{0.75}\cdot\Delta\mathrm{BR}$ $(\mathrm{B}_J^* \to \mathrm{B}^{(*)}\pi\pi)$
$\mathrm{BR}(\mathrm{B}_{J\,\mathrm{broad}}^* \to \mathrm{B}^*\pi)$	$+0.059$	-0.0015	-4.8	$+0.0097$	$+1$	$+0.011$
$\Gamma(\mathrm{B}_2^*)/\Gamma(\mathrm{B}_1(3/2))$	$+0.014\atop-0.009$	$+0.0008\atop-0.0013$	$+4.1\atop-1.9$	$+0.0001\atop-0.0029$	$+2\atop-0$	$+0.007\atop-0.016$
$\Gamma(\mathrm{B}_1(1/2))/\Gamma(\mathrm{B}_0^*)$	$+0.001$	$+0.0004$	$+0.5$	-0.0030	-20	-0.004
$\mathrm{f}_{\mathrm{narrow}}$	$+0.049\atop-0.028$	$+0.0001\atop-0.0002$	$+7.9\atop-8.9$	$+0.0144\atop-0.0199$	±12	$+0.001\atop-0.008$
prod. rate $\mathrm{B}_1(3/2)$ vs. B_2^*	±0.012	$+0.0015\atop-0.0021$	±1.2	$+0.0000\atop-0.0022$	±1	$+0.003\atop-0.006$
prod. rate B_0^* vs. $\mathrm{B}_1(1/2)$	$+0.004\atop-0.003$	$+0.0001\atop-0.0002$	±0.0	$+0.0060\atop-0.0054$	$+1\atop-2$	$+0.003\atop-0.002$
$\mathrm{BR}(\mathrm{B}_2^* \to \mathrm{B}^*\pi/\mathrm{B}\pi)$	$+0.013\atop-0.008$	$+0.0012\atop-0.0004$	$+2.4\atop-1.2$	$+0.0043\atop-0.0075$	$+3\atop-2$	$+0.012\atop-0.017$
$M(\mathrm{B}_2^*) - M(\mathrm{B}_1(3/2))$	$+0.003\atop-0.002$	±0.0024	$+2.4\atop-3.2$	$+0.0017\atop-0.0010$	±2	$+0.003\atop-0.002$
$M(\mathrm{B}_1(1/2)) - M(\mathrm{B}_0^*)$	±0.001	±0.0001	$+0.0\atop-0.2$	$+0.0119\atop-0.0200$	$+5\atop-6$	$+0.007\atop-0.012$
efficiency $f(M(\mathrm{B}\pi))$	±0.039	±0.0018	±4.3	±0.0050	±1	±0.109
reweighting of $N_{\gamma_{\mathrm{ECAL}}}$	±0.036	±0.0021	±7.4	±0.0025	±2	±0.021
B^* efficiency (ECAL)	$+0.013\atop-0.023$	$+0.0007\atop-0.0005$	$+1.3\atop-2.3$	$+0.0004\atop-0.0016$	$+1$	±0.003
efficiency $f(\cos\theta^*)$	$+0.002\atop-0.001$	$+0.001\atop-0.0002$	$+4.1\atop-5.0$	$+0.0077\atop-0.0103$	$+6\atop-7$	$+0.002\atop-0.004$
sideband norm. B^*-enr.	$+0.125\atop-0.071$	$+0.0041\atop-0.0032$	$+15.0\atop-9.3$	$+0.0013\atop-0.0020$	$+3\atop-6$	$+0.017\atop-0.010$
sideband norm. B^*-dep.	$+0.116\atop-0.067$	$+0.0031\atop-0.0025$	$+9.6\atop-4.5$	$+0.0075\atop-0.0081$	$+4\atop-9$	$+0.014\atop-0.022$
Peterson fragmentation	$+0.034\atop-0.049$	$+0.0010\atop-0.0008$	$+12.3\atop-6.4$	$+0.0044\atop-0.0047$	$+35\atop-27$	$+0.046\atop-0.065$
background fit function	±0.023	±0.0025	±0.6	±0.0055	±6	±0.005
sideband range variation	$+0.032\atop-0.030$	$+0.0012\atop-0.0011$	$+3.9\atop-5.2$	$+0.0037\atop-0.0064$	$+5\atop-13$	$+0.005\atop-0.007$
B decay bg fraction	$+0.037\atop-0.044$	$+0.0001\atop-0.0008$	$+4.7\atop-5.0$	$+0.0089\atop-0.0082$	$+4\atop-6$	±0.054
B decay bg modelling	±0.016	±0.0012	±6.9	±0.0111	±25	±0.002
b fragm. bg fraction	$+0.030\atop-0.028$	$+0.0003\atop-0.0004$	$+5.7\atop-4.4$	$+0.0060\atop-0.0084$	$+10\atop-8$	$+0.042\atop-0.061$
b fragm. bg modelling	±0.025	±0.0002	±4.7	±0.0104	±33	±0.007
udsc bg fraction	±0.023	$+0.0001\atop-0.0000$	±0.5	±0.0007	±0	±0.002
variation of bin width	$+0.009\atop-0.005$	$+0.0010\atop-0.0008$	$+5.0\atop-3.5$	$+0.0044\atop-0.0076$	$+5\atop-16$	$+0.017\atop-0.033$
$\mathrm{B}^{(*)\prime}$ contamination	$+0.026\atop-0.028$	$+0.0003\atop-0.0002$	$+3.5\atop-3.7$	$+0.0055\atop-0.0044$	$+4\atop-5$	±0.003
B_{sJ}^* contamination	±0.021	$+0.0002\atop-0.0004$	±2.7	$+0.0042\atop-0.0043$	±4	$+0.004\atop-0.005$
variation of fit range	±0.002	$+0.0001\atop-0.0000$	$+2.0\atop-1.7$	$+0.0009\atop-0.0006$	$+11\atop-10$	$+0.010\atop-0.006$
total	$+0.21\atop-0.15$	±0.007	$+29\atop-23$	$+0.034\atop-0.042$	±63	$+0.143\atop-0.161$
central value of fit result	0.74	5.738	18	5.839	129	0.327

Table 7: Systematic errors on the fit parameters of the simultaneous fit. The numbers for $\Delta\mathrm{BR}(\mathrm{B}_J^* \to \mathrm{B}^{(*)}\pi\pi)$ have to be multiplied by 0.75 to account for double counting. The total systematic error of each fit parameter is the quadratic sum of the individual errors. Sources of systematic uncertainty with an error of smaller than 10% of the total systematic error for *each* fit parameter are excluded from the table.

8.2.4 Contamination of the B_J^* signal, other uncertainties and cross checks

- Contributions from higher orbital or radial excitations of B mesons decaying to $B^{(*)}\pi$ or $B^{(*)}\pi\pi$ may be contained in the signal peaks of the B^*-enriched and the B^*-depleted samples. The procedure described in Section 8.1.1 is repeated.

- Reflections from B_{sJ}^* decays influence the fit results since a small fraction of kaons are misidentified as pions. The B_{sJ}^* production rate is varied by $\pm 50\%$ to cover the experimental error [5].

- The range of the fit region is changed by ± 80 MeV/c^2 on both sides.

- The whole analysis is performed using bin widths of 16 and 25 MeV/c^2 instead of 20 MeV/c^2.

- A fit to total $B\pi^{\pm}$ mass spectrum produces results for $M(B_1(3/2))$, $\Gamma(B_1(3/2))$, $M(B_0^*)$, $\Gamma(B_0^*)$ and $BR(B_J^* \to B^{(*)}\pi\pi)$ in good agreement with the fit results obtained from the mass spectra of the B^*-enriched and B^*-depleted samples. Furthermore, the fit to the total $B\pi$ mass spectrum is repeated with f_{narrow} as an additional fit parameter. The result $f_{\text{narrow}} = 0.76\,^{+\,0.11}_{-\,0.24}\,_{\text{stat}}$ is in agreement with the fixed value of 0.6 used in the original fit.

- The number of B_J^* signal entries observed in Figure 7 and the Monte Carlo reconstruction efficiencies produce a total B_J^* production rate consistent with our measurement presented in [5].

8.2.5 Robustness of fit results

Extensive systematic studies have been performed to test the stability of the fit results. Since the systematic error on $BR(B_J^* \to B^{(*)}\pi\pi)$ is large, the existence of $B_J^* \to B^{(*)}\pi\pi$ decays can be questioned and the fit is repeated with $BR(B_J^* \to B^{(*)}\pi\pi) = 0$. Furthermore, the functional form of the broad B_J^* states, which is not precisely known at $B\pi$ threshold, has been varied assuming different theoretical approaches. The fit probability for any fit with $BR(B_J^* \to B^{(*)}\pi\pi)$ fixed to zero is always below 4% (to be compared with a fit probability of 65% of the original fit). Depending on the functional form of the broad B_J^* states, the mass of the broad B_J^* states lies below or above the $B_1(3/2)$ mass for $BR(B_J^* \to B^{(*)}\pi\pi) = 0$. Because of this ambiguity, the widths and the mass of the B_0^* as well as $BR(B_J^* \to B^{(*)}\pi\pi)$ are not quoted as robust fit results. The mass and the width of the $B_1(3/2)$ as well as $BR(B_J^* \to B^*\pi)$ stay stable for all fits. The described ambiguity is also observed in the corresponding fit to the total $B\pi$ mass spectrum. In comparison to other measurements, especially [10], this is a rather conservative treatment of the fit results. Experiments with comparable mass resolution are expected to have similar problems in determining B_J^* properties from a fit to a single $B\pi$ mass peak.

9 Summary and conclusion

We have analysed orbitally-excited mesons by forming combinations of inclusively reconstructed B mesons and charged pions. A new way to determine the combinatorial $B\pi$ background using data test samples while maintaining high statistics is presented. A high statistics tag of the decay $B^* \to B\gamma$ is used to obtain B_J^* samples enriched or depleted in their B^* content. We

present the first measurement of the branching ratio of orbitally-excited B mesons decaying into B*. The result is

$$\mathrm{BR}(\mathrm{B}_J^* \to \mathrm{B}^*\pi(X)) = 0.85 \,{}^{+0.26}_{-0.27} \pm 0.12 \,,$$

where the first error is statistical and the second systematic. The measurement does not depend on the shape of $\mathrm{B}\pi$ mass distributions or on any specific model. It is in agreement with theoretical predictions and the measured B* and B_J^* production rates at LEP.

Making further use of the B* information, a simultaneous fit to the B_J^* mass spectra of samples enriched or depleted in their B* content is performed. In this fit, the masses, widths and production rates of the $\mathrm{B}_1(1/2)$ and B_2^* are constrained by the corresponding properties of their doublet partners B_0^* and $\mathrm{B}_1(3/2)$, respectively. The fit yields

$$
\begin{aligned}
M(\mathrm{B}_1(3/2)) &= (\, 5.738 \,{}^{+\,0.005}_{-\,0.006} \pm 0.007 \,)\ \mathrm{GeV}/c^2 \\
\Gamma(\mathrm{B}_1(3/2)) &= (\, 18 \,{}^{+\,15\,+\,29}_{-\,13\,-\,23} \,)\ \mathrm{MeV}/c^2 \\
\mathrm{BR}(\mathrm{B}_J^* \to \mathrm{B}^*\pi) &= 0.74 \,{}^{+\,0.12\,+\,0.21}_{-\,0.10\,-\,0.15} \,.
\end{aligned}
$$

The first error indicates the statistical and the second error the systematic uncertainty. The fit favours a contribution of $\mathrm{B}_J^* \to \mathrm{B}^{(*)}\pi\pi$ decays to the B_J^* signal and a mass of the broad B_J^* states about 100 MeV/c^2 above the narrow B_J^* states. Systematic uncertainties in the reconstruction efficiency and the combinatorial background at low $\mathrm{B}\pi$ masses together with the lack of knowledge of the exact functional form of the broad B_J^* states at $\mathrm{B}\pi$ threshold do not allow an unambiguous determination of the width and mass of the B_0^* (or $\mathrm{B}_1(1/2)$). The fit results are in agreement with predictions from several HQET models. The $M(\mathrm{B}_1(3/2))$ result agrees well with a measurement of $M(\mathrm{B}_2^*)$ [8]. On the other hand, a recent B_J^* analysis [10] presented masses that disagree with the results of this analysis and with [8]. The measured value of $\mathrm{BR}(\mathrm{B}_J^* \to \mathrm{B}^{(*)}\pi\pi) = 0.25 \pm 0.02 \,{}^{+\,0.11}_{-\,0.12}$ is consistent with the range 0.1-0.2 predicted by theory [4] and in agreement with an experimental result obtained from the reconstruction of the $\mathrm{B}^{(*)}\pi\pi$ final state [33]. The results for $\mathrm{BR}(\mathrm{B}_J^* \to \mathrm{B}^*\pi(X))$, $\mathrm{BR}(\mathrm{B}_J^* \to \mathrm{B}^*\pi)$ and $\mathrm{BR}(\mathrm{B}_J^* \to \mathrm{B}^{(*)}\pi\pi)$ are in good agreement with each other on the assumption that the decay channels with $X \neq \pi$ contributing to $\mathrm{BR}(\mathrm{B}_J^* \to \mathrm{B}^*\pi(X))$ are small.

References

[1] M. Voloshin and M. Shifman, Sov. J. Nucl. Phys. 45 (1987) 292;
    M. Voloshin and M. Shifman, Sov. J. Nucl. Phys. 47 (1988) 511;
    S. Nussinov and W. Wetzel, Phys. Rev. D36 (1987) 130;
    N. Isgur and M.B. Wise, Phys. Lett. B232 (1989) 113;
    N. Isgur and M.B. Wise, Phys. Lett. B237 (1990) 527;
    N. Isgur and M.B. Wise, Phys. Rev. Lett. 66 (1991) 1130;
    E. Eichten and B. Hill, Phys. Lett. B234 (1990) 511;
    B. Grinstein, Nucl. Phys. B339 (1990) 253;
    H. Georgi, Phys. Lett. B240 (1990) 447;
    A. Falk, H. Georgi, B. Grinstein, M. Wise, Nucl. Phys. B343 (1990) 1;
    J.D. Bjorken, I. David, J. Taron, Nucl. Phys. B371 (1990) 111.

[2] Particle Data Group, C. Caso et al., Eur. Phys. J. C3 (1998) 1.

[3] S. Godfrey and R. Kokoski, Phys. Rev. D43 (1991) 1679.

[4] E.J. Eichten, C.T. Hill, C. Quigg, Phys. Rev. Lett. 71 (1993) 4116;
    E.J. Eichten, C.T. Hill, C. Quigg, FERMILAB-CONF-94-117-T, May 1994.

[5] OPAL collaboration, G. Alexander et al., Z. Phys. C66 (1995) 19.

[6] DELPHI collaboration, P. Abreu et al., Phys. Lett. B345 (1995) 598.

[7] ALEPH collaboration, D. Buskulic et al., Z. Phys. C69 (1996) 393.

[8] ALEPH collaboration, R. Barate et al., Phys. Lett. B425 (1998) 215.

[9] CDF collaboration, T. Affolder et al., FERMILAB-PUB-99-330-E (1999), submitted to
    Phys. Rev. D.

[10] L3 collaboration, M. Acciarri et al., Phys. Lett. B465 (1999) 323.

[11] D. Ebert, V.O. Galkin, R.N. Faustov, Phys. Rev. D57 (1998) 5663;
    Erratum Phys. Rev. D59 (1999) 019902.

[12] S. Godfrey and N. Isgur, Phys. Rev. D32 (1985) 189;
    M. Gronau and J. Rosner, Phys. Rev. D49 (1994) 254;
    N. Gupta and J.M. Johnson, Phys. Rev. D51 (1994) 168;
    A.F. Falk and T. Mehen, Phys. Rev. D53 (1996) 231;
    Y.-B. Dai and S.-L. Zhu, Phys. Rev. D58 (1998) 074009;
    Y.-B. Dai, C.-S. Huang, M.-Q. Huang, H.-Y. Jin, C. Liu, Phys. Rev. D58 (1998) 094032.

[13] N. Isgur, Phys. Rev. D57 (1998) 4041.

[14] A.H. Orsland and H. Hogaasen, Eur. Phys. J. C9 (1999) 503.

[15] P.P. Allport et al., Nucl. Instr. Meth. A346 (1994) 476.

[16] OPAL collaboration, K. Ahmet et al., Nucl. Instr. Meth. A305 (1991) 275;
     P.P. Allport et al., Nucl. Instr. Meth. A324 (1993) 34.

[17] OPAL collaboration, G. Alexander et al., Z. Phys. C52 (1991) 175.

[18] T. Sjöstrand, Comp. Phys. Comm. 82 (1994) 74.

[19] OPAL collaboration, G. Alexander et al., Z. Phys. C69 (1996) 543.

[20] C. Peterson, D. Schlatter, I. Schmitt and P. Zerwas, Phys. Rev. D27 (1983) 105.

[21] J. Allison et al., Nucl. Instr. Meth. A317 (1992) 47.

[22] OPAL collaboration, K. Ackerstaff et al., Z. Phys. C74 (1997) 413.

[23] N. Brown and W.J. Stirling, Phys. Lett. B252 (1990) 657;
     S. Bethke, Z. Kunszt, D. Soper and W.J. Stirling, Nucl. Phys. B370 (1992) 310;
     S. Catani et al., Phys. Lett. B269 (1991) 432;
     N. Brown and W.J. Stirling, Z. Phys. C53 (1992) 629.

[24] OPAL Collaboration, K. Ackerstaff et al., Eur. Phys. J. C2 (1998) 213.

[25] OPAL Collaboration, G. Abbiendi et al., Eur. Phys. J. C7 (1999) 407.

[26] OPAL collaboration, R. Akers et al., Z. Phys. C63 (1994) 197.

[27] The neural networks were trained using JETNET 3:
     C. Peterson, T. Rögnvaldsson and L. Lönnblad, Comp. Phys. Comm. 81 (1994) 185.

[28] A similar neural network has already been used in:
     OPAL Collaboration, G. Abbiendi et al., Eur. Phys. J. C8 (1999) 217.

[29] OPAL collaboration, K. Ackerstaff et al., Eur. Phys. J. C5 (1998) 411;
     OPAL collaboration, K. Ackerstaff et al., Z. Phys. C74 (1997) 413;
     OPAL collaboration, G. Alexander et al., Z. Phys. C73 (1997) 587;
     OPAL collaboration, G. Alexander et al., Z. Phys. C70 (1996) 357.

[30] OPAL collaboration, K. Ackerstaff et al., Eur. Phys. J. C5 (1998) 411.

[31] OPAL collaboration, R. Akers et al., Phys. Lett. B316 (1993) 435.

[32] G. Eigen, Int. J. Mod. Phys. A12 (1997) 3909;
     R. Kokoski and N. Isgur, Phys. Rev. D35 (1987) 907.

[33] G. Eigen, Int. J. Mod. Phys. A12 (1997) 3909;
     M.-L. Andrieux, Nucl. Phys. B Proc. Suppl. 55A (1997) 51;
     F. Ledroit, Nucl. Phys. B Proc. Suppl. 64 (1998) 411.

[34] CLEO collaboration, S. Anderson et al., *Observation of a Broad L = 1 c$\bar{q}$ State in* B$^-$ $\rightarrow$ D$^{*+}\pi^-\pi^-$ *at CLEO*, CLEO-CONF-99-6, August 1999.

[35] Threshold factors of this type can be found in:
PYTHIA (version 6.1): T. Sjöstrand, Comp. Phys. Comm. 82 (1994) 74.

[36] For the fits the MINUIT package is used:
MINUIT (release 96.03): F. James and M. Roos, Comput. Phys. Commun. 10 (1975) 343.

[37] A.F. Falk and M.E. Peskin, Phys. Rev. D49 (1994) 3320.

[38] OPAL collaboration, G. Abbiendi et al., Eur. Phys. J. C8 (1999) 573.

[39] DELPHI collaboration, P. Abreu et al., Phys. Lett. B425 (1998) 399;
L3 collaboration, M. Acciari et al., Phys. Lett. B416 (1998) 220;
OPAL collaboration, R. Akers et al., Z. Phys. C61 (1994) 209.
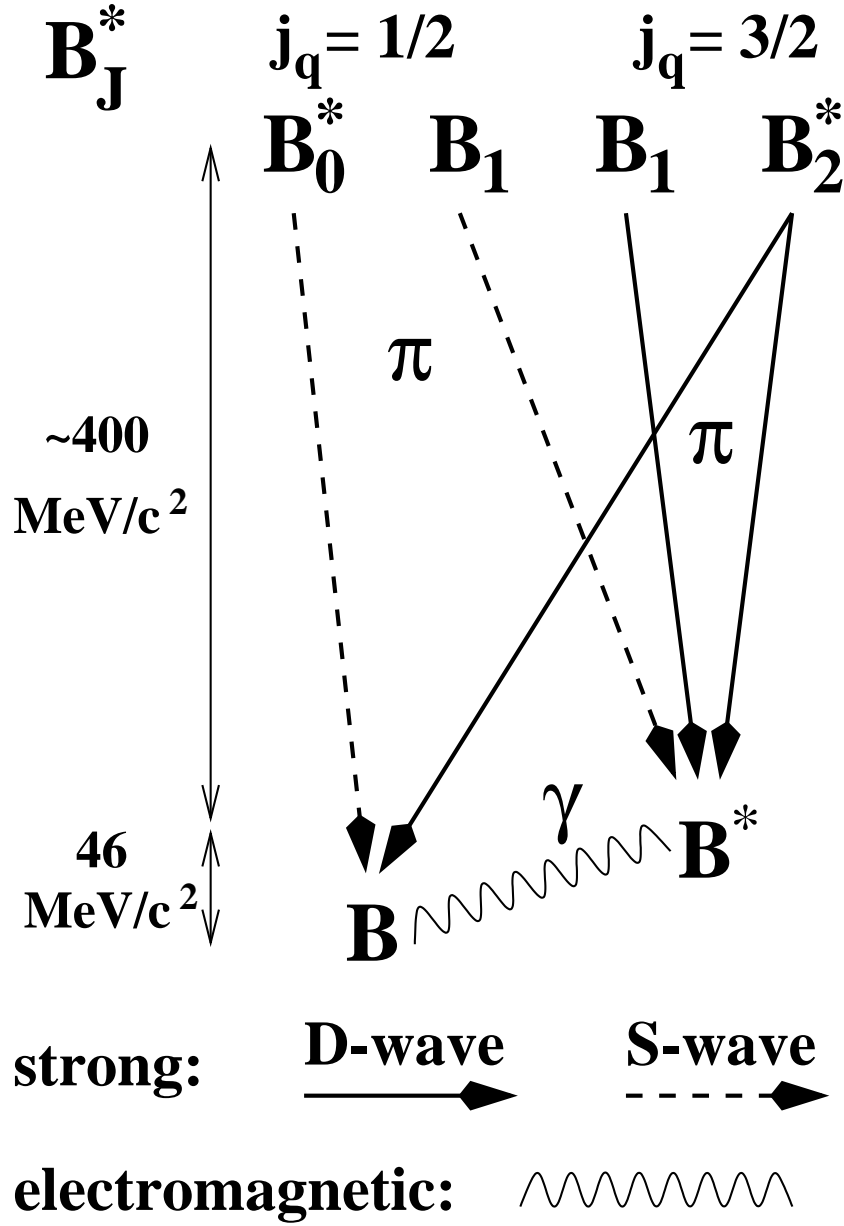
Figure 1:   The four B_J^* states and their dominant decays to the ground state doublet (B, B^*). Strong decays via single pion emission are indicated as solid (D-wave) and dashed (S-wave) lines. The B^* decays radiatively because of the small B^*–B mass splitting.

OPAL
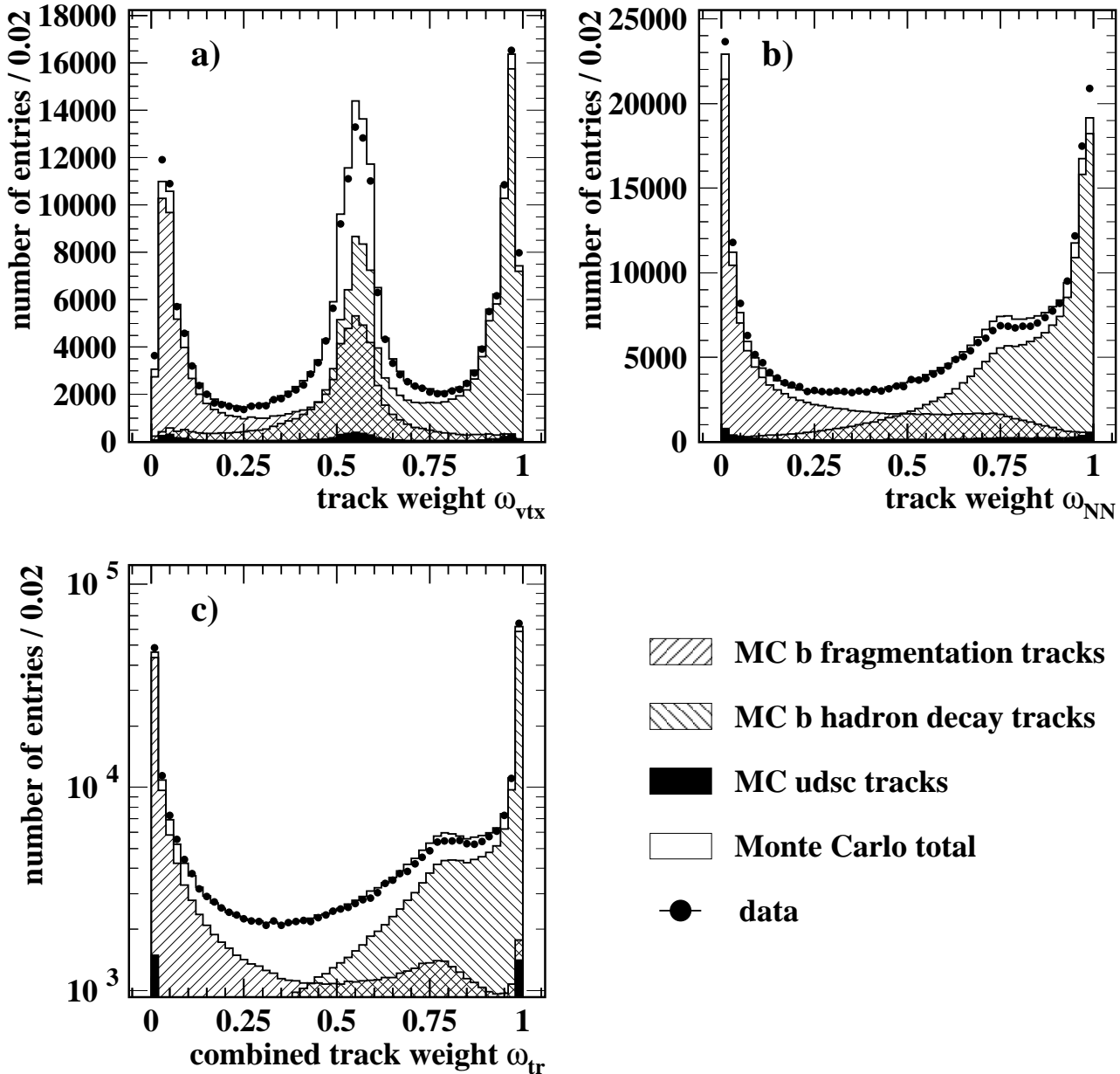
Figure 2: a) The track weight ω_{vtx} for all tracks in hemispheres with a good secondary vertex. The peaks near 0 and 1 correspond to tracks created by b fragmentation and b hadron decay tracks, respectively. The peak near 0.5 is produced by tracks which are not unambiguously assigned to the primary or the secondary vertex, as in the case of tracks matching both the primary and secondary vertex or matching no vertex at all. b) The track weight ω_{NN} for tracks of all hemispheres (with or without a good secondary vertex). The separation power of ω_{NN} is superior to the separation power of ω_{vtx}. c) The combined track weight ω_{tr} calculated from ω_{vtx} and ω_{NN} for tracks of all hemispheres. Note that ω_{tr} is shown on a logarithmic scale.

OPAL
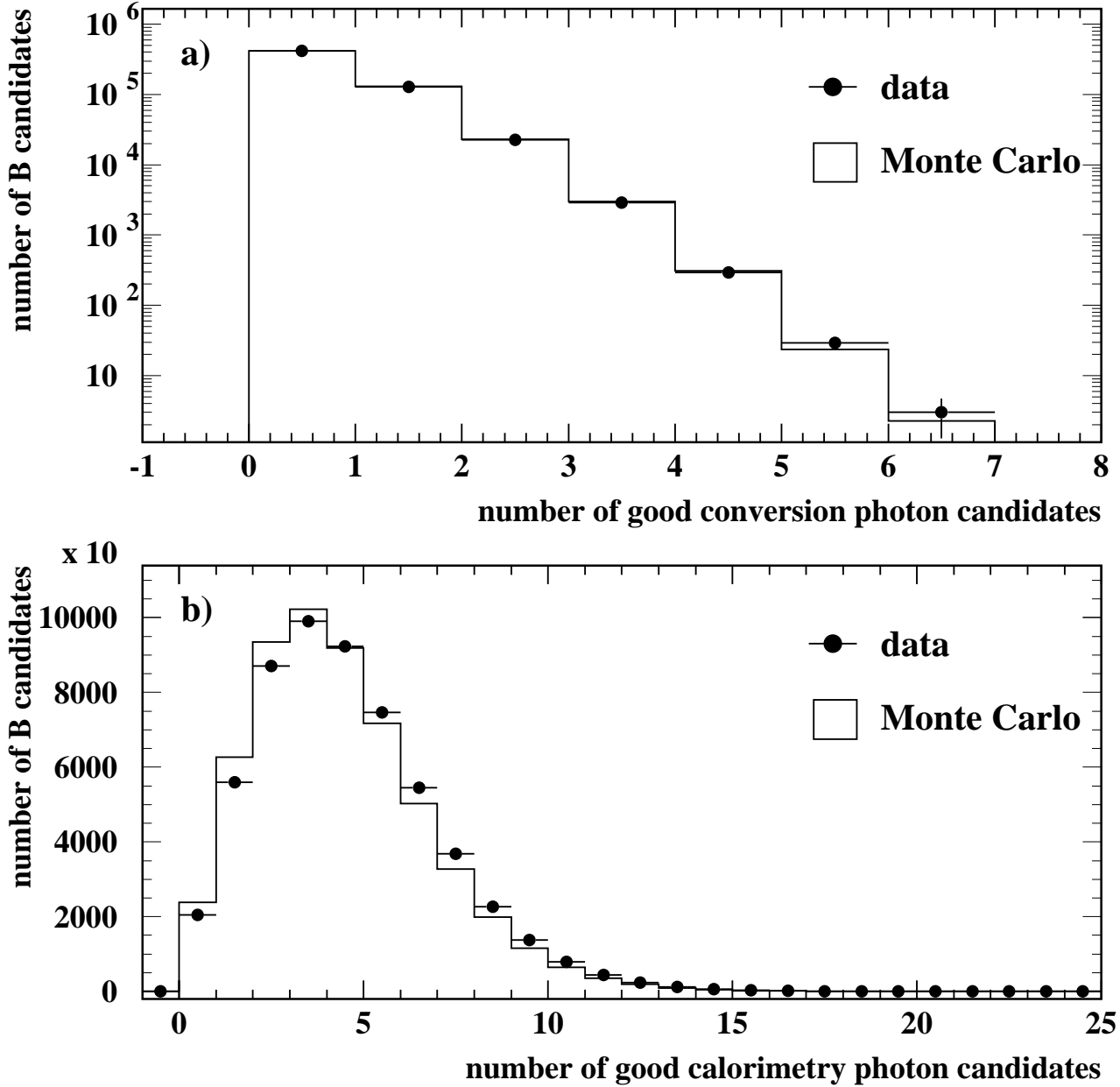
Figure 3: a) The number of good conversion photon candidates per B candidate observed in data and Monte Carlo. b) The number of good calorimeter photon candidates per B candidate observed in data and Monte Carlo. For the analysis, the Monte Carlo distribution of the latter is reweighted to the data distribution.

OPAL
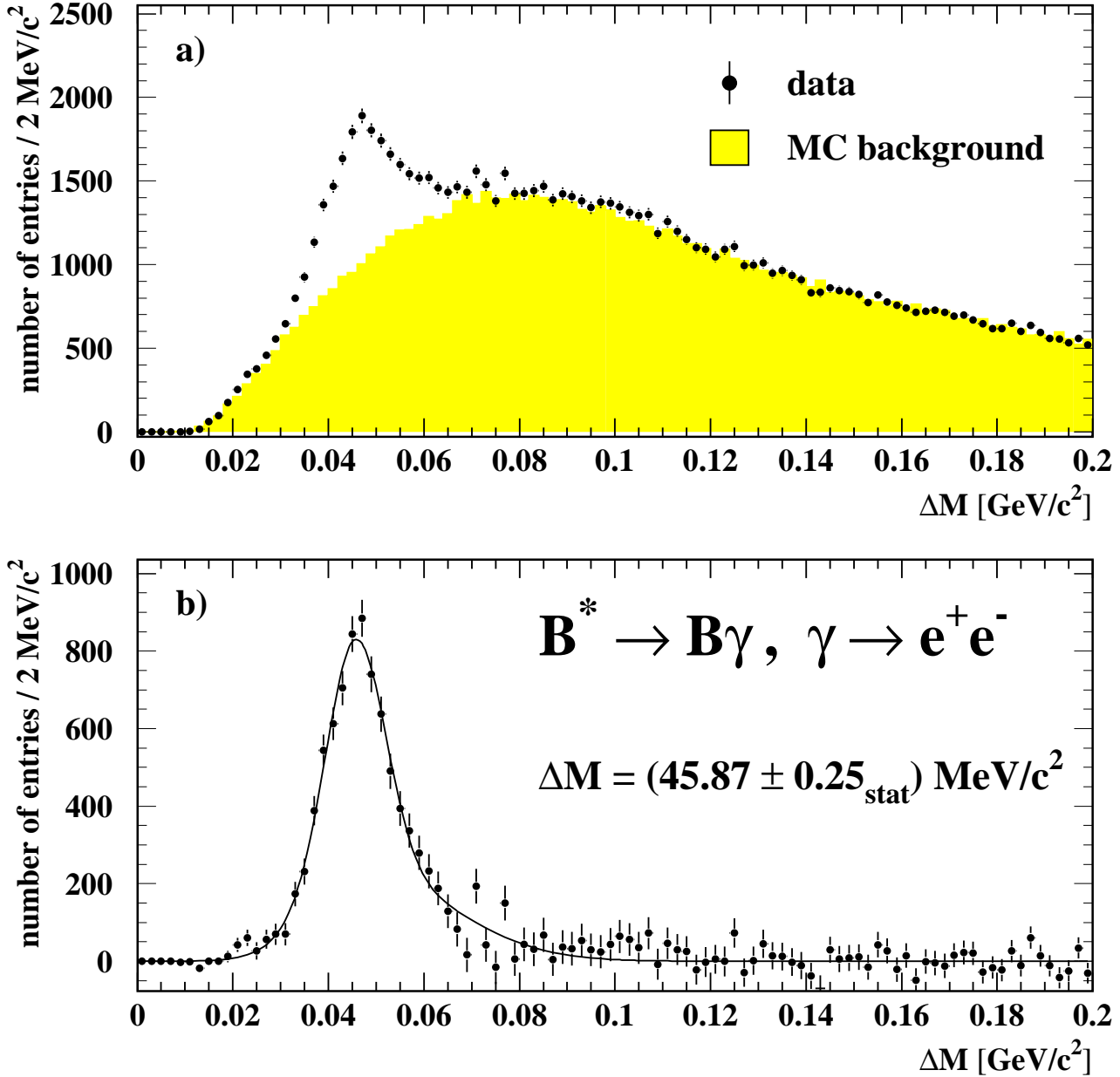
Figure 4: a) The $\Delta M = M_{B\gamma} - M_B$ mass distribution of the conversion photon sample. The background is estimated from Monte Carlo simulation and normalised to the data distribution in the sideband region 0.09 GeV/$c^2 < \Delta M < 0.20$ GeV/c^2. b) The corresponding background subtracted signal. The fit function used for the signal is described in the text.
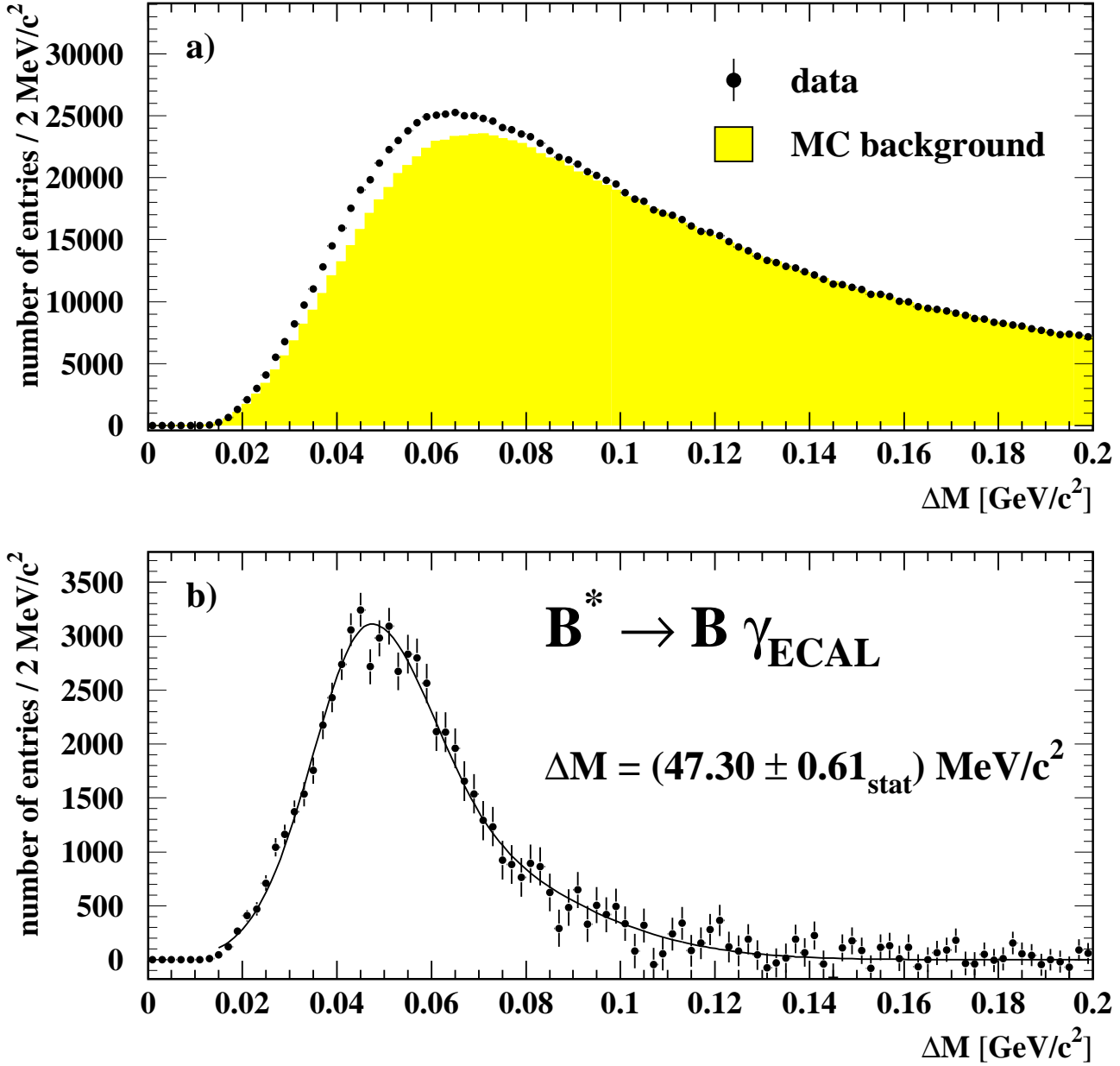
Figure 5: a) The $\Delta M = M_{B\gamma} - M_B$ mass distribution of photons reconstructed in the electromagnetic calorimeter. The background is estimated from the Monte Carlo simulation and normalised to the data distribution in the sideband region $0.10\ \mathrm{GeV}/c^2 < \Delta M < 0.20\ \mathrm{GeV}/c^2$. Although the resolution is poor compared to the conversion photon sample, an excess of entries in the data distribution around $46\ \mathrm{MeV}/c^2$ is clearly visible. b) The corresponding background subtracted signal. The fit function is described in the text.

OPAL
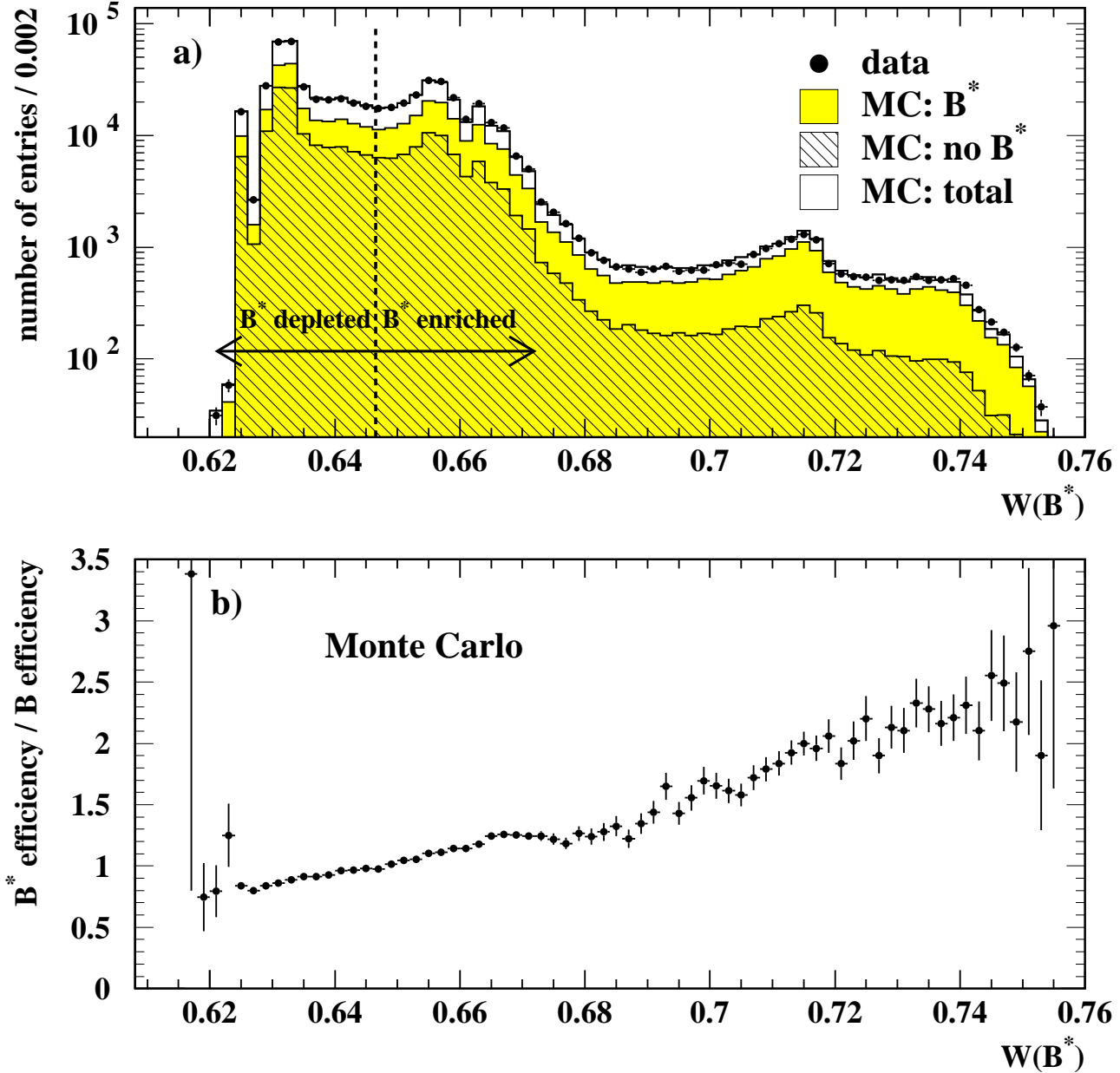
Figure 6: a) The $\mathcal{W}(B^*)$ distribution for data with the corresponding Monte Carlo histograms indicating the number of B candidates with a B* parent and no B* parent. The dotted line gives the boundary between the B*-enriched and B*-depleted samples. b) The ratio of the efficiency to reconstruct a B meson with a B* parent over the efficiency to reconstruct a B meson without a B* parent versus the weight $\mathcal{W}(B^*)$ calculated from simulated data.

OPAL
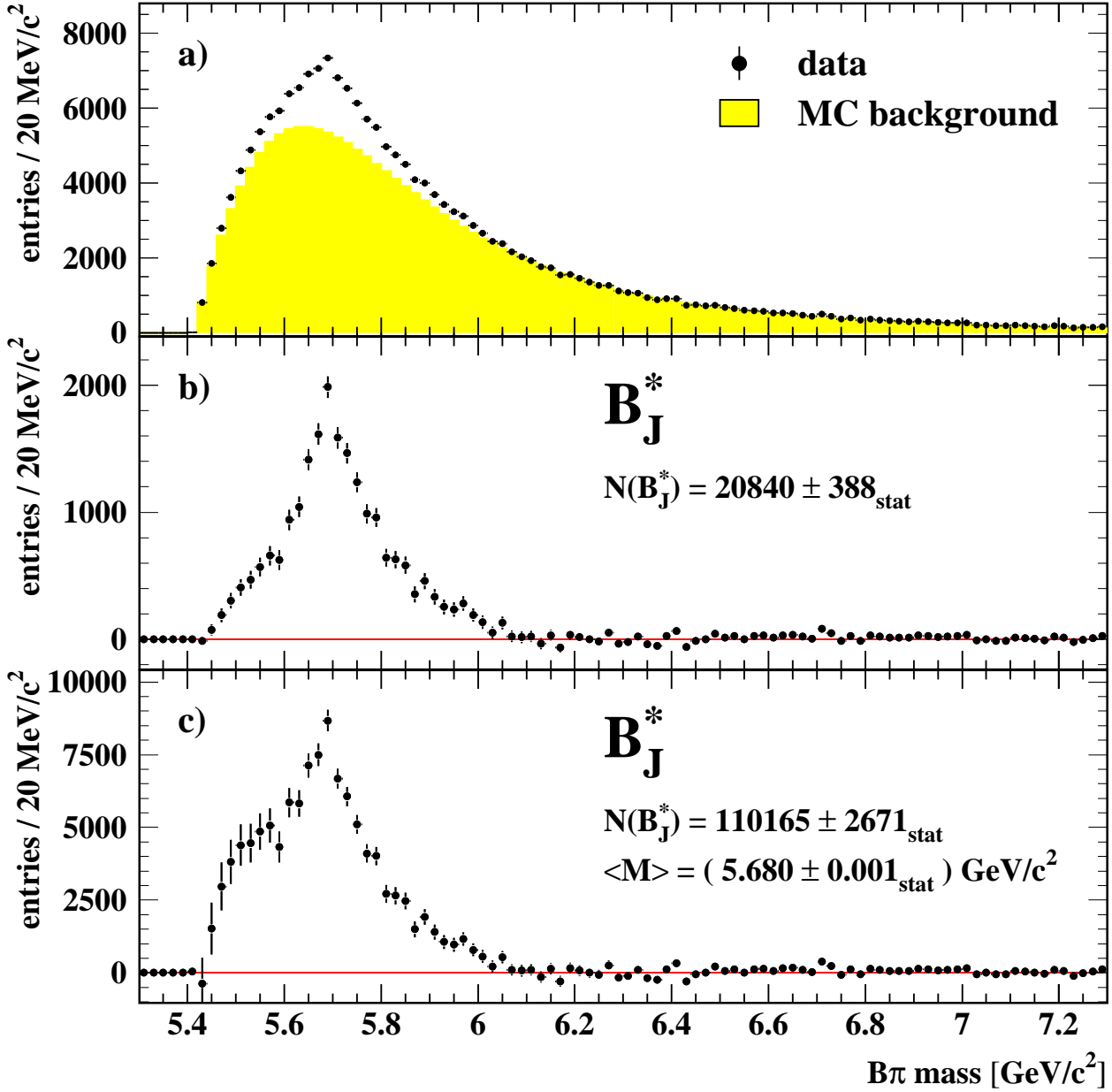
Figure 7: a) The $B\pi^{\pm}$ mass distribution for data. The shaded histogram indicates a fit to the corrected Monte Carlo background using a reweighting method described in Section 8.1.2. The function used for the fit is described in the text. b) The B_J^* signal after subtraction of the simulated background. c) The efficiency-corrected B_J^* signal. The observed structure of the B_J^* signal suggests a superposition of several different states. The mass dependent efficiency correction has a strong impact on the signal shape at low $B\pi$ mass values.

OPAL Monte Carlo
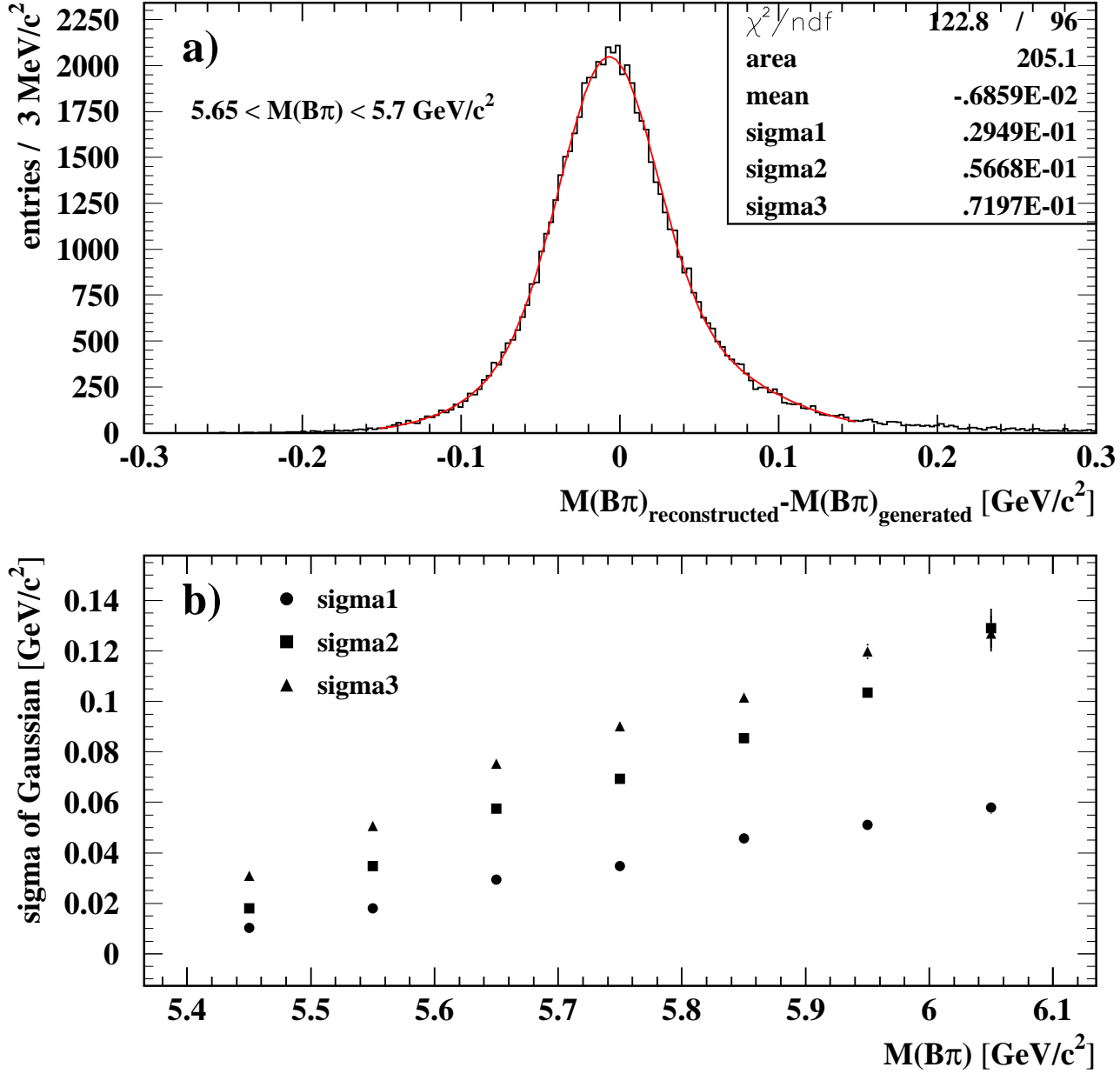
Figure 8: a) Monte Carlo $M_{B\pi}$ resolution of B^*_J decaying to $B^{(*)}\pi^{\pm}$ in the mass region $5.65\ \mathrm{GeV}/c^2 < M(B\pi) < 5.70\ \mathrm{GeV}/c^2$. The fit function is the sum of two Gaussians both constrained to the same mean value. Sigma1 is the standard deviation of the narrow Gaussian and sigma2 (sigma3) corresponds to the left (right) standard deviation of the asymmetric broad Gaussian. b) The linear dependence of the width of the resolution function on $M_{B\pi}$ is shown for each sigma in the B^*_J signal region.
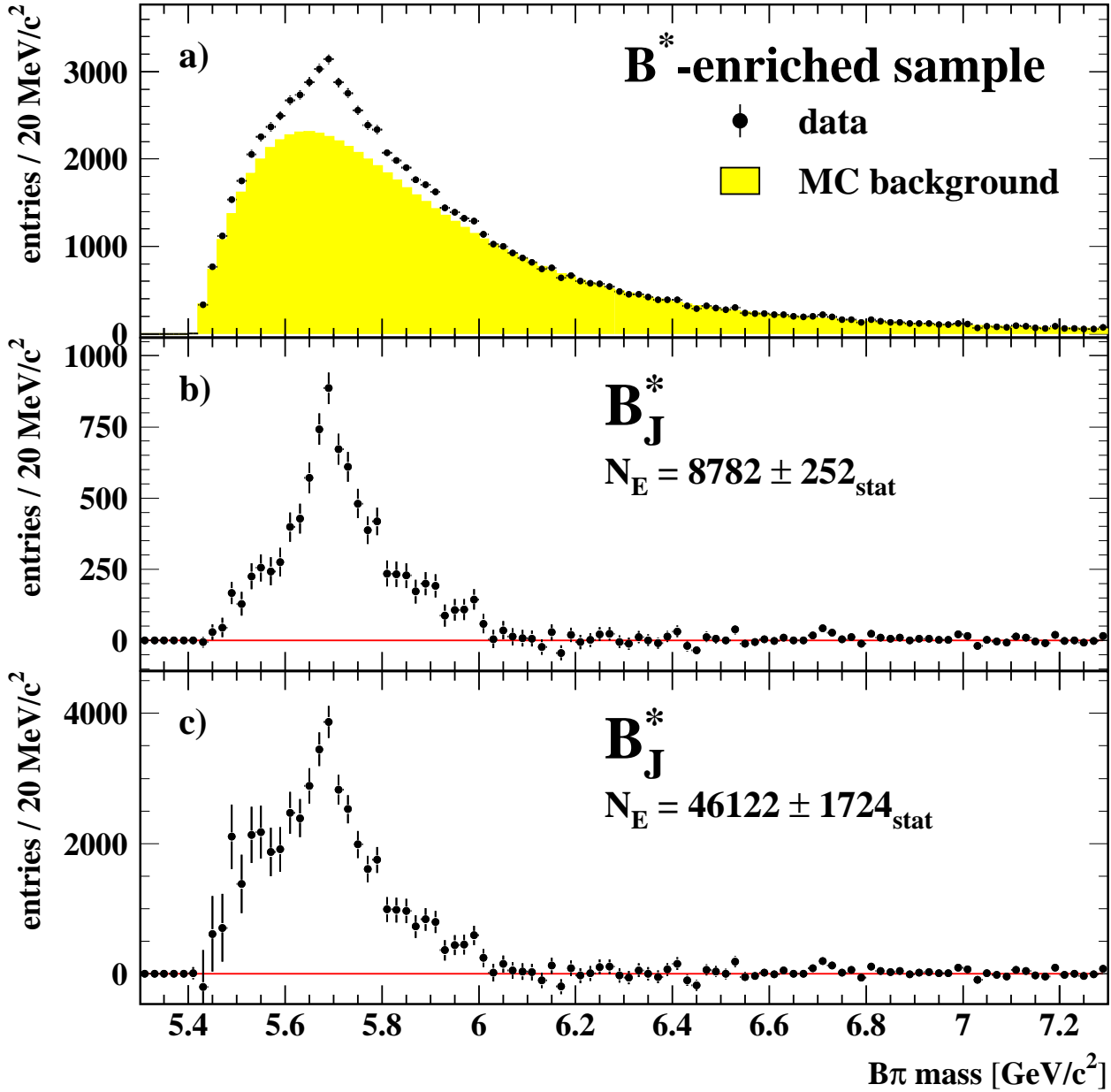
Figure 9: a) The B$\pi^{\pm}$ mass distribution of the sample enriched in the decay B$_J^*\rightarrow$ B$^*\pi^{\pm}(X)$ in data. The shaded histogram indicates a fit to the corrected Monte Carlo background using a reweighting method described in Section 8.1.2. b) The signal distribution after subtraction of the simulated background. c) The efficiency-corrected signal.
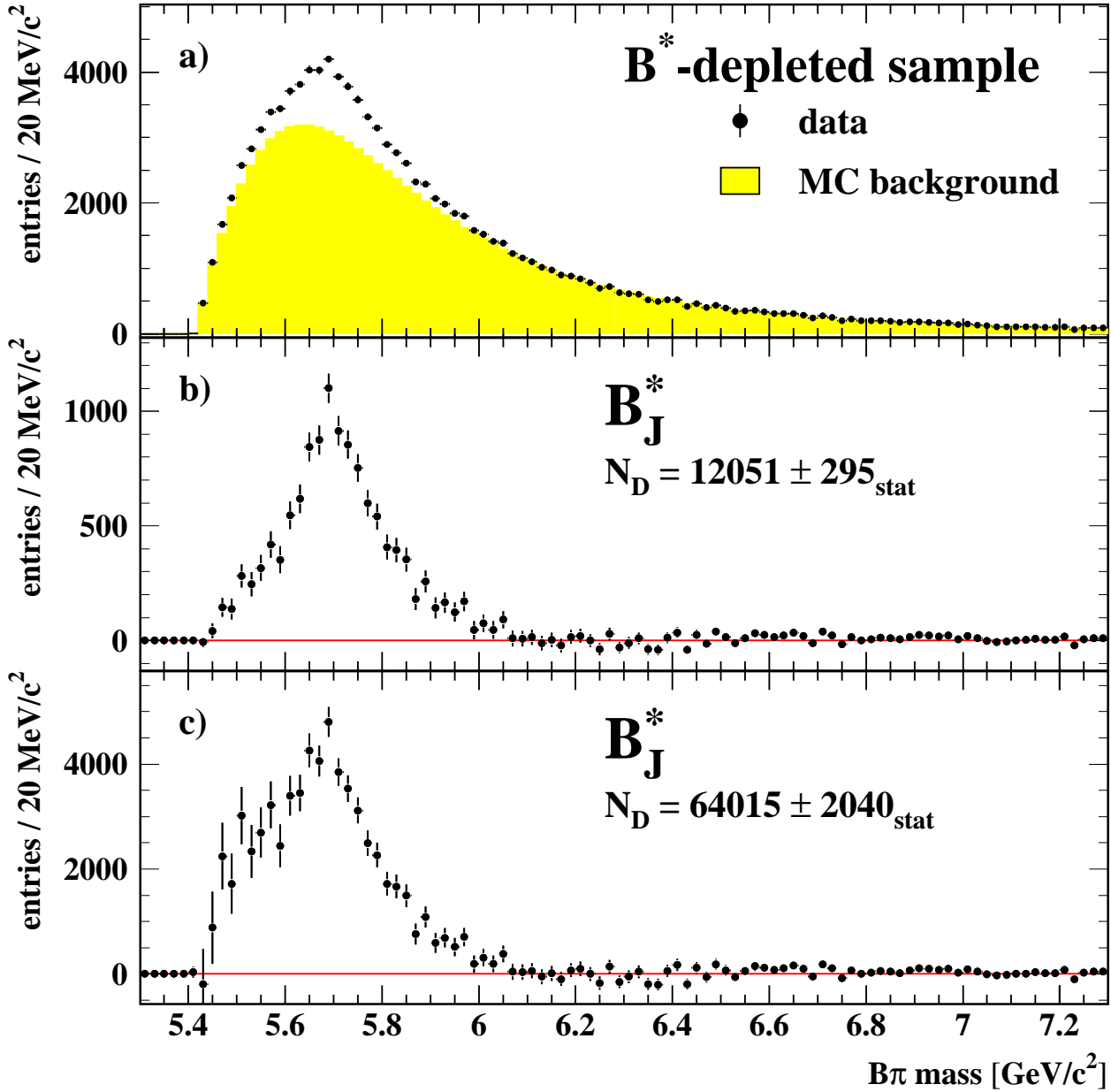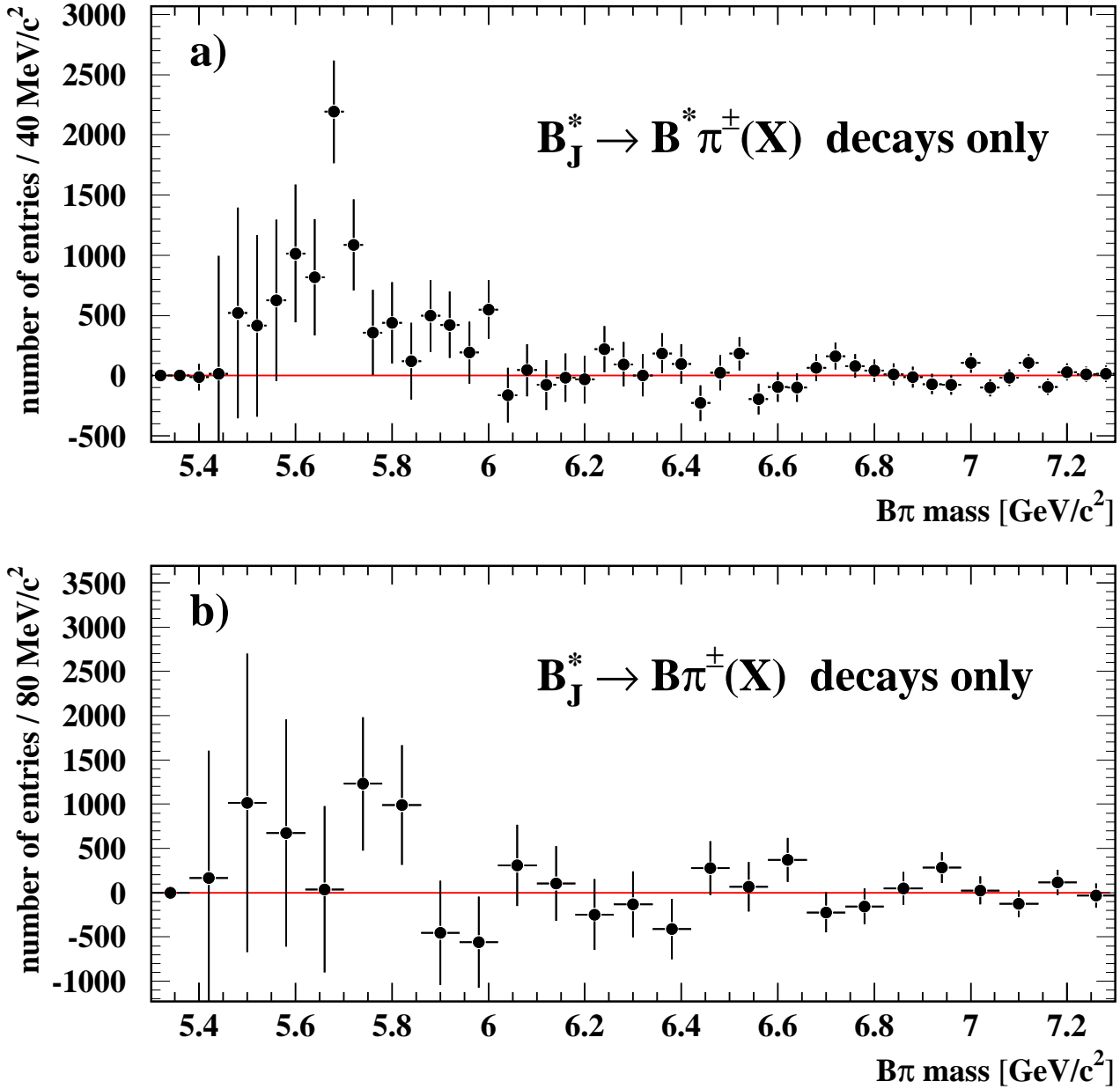
OPAL

Figure 10: a) The $B\pi^\pm$ mass distribution of the sample depleted in the decay $B^*_J \to B^*\pi^\pm(X)$ in data. The shaded histogram indicates a fit to the corrected Monte Carlo background using a reweighting method described in Section 8.1.2. b) The signal distribution after subtraction of the simulated background. c) The efficiency-corrected signal.

Figure 11: a) The efficiency-corrected $B\pi^{\pm}$ mass distribution of $B_J^* \to B^*\pi^{\pm}(X)$ transitions seen in data. A clear peak is visible at 5.7 GeV/c^2. The structure is unlikely to stem from a single state. b) The efficiency-corrected $B\pi^{\pm}$ mass distribution of $B_J^* \to B\pi^{\pm}(X)$ transitions seen in data. A 2.2σ excess is observed around 5.8 GeV/c^2.
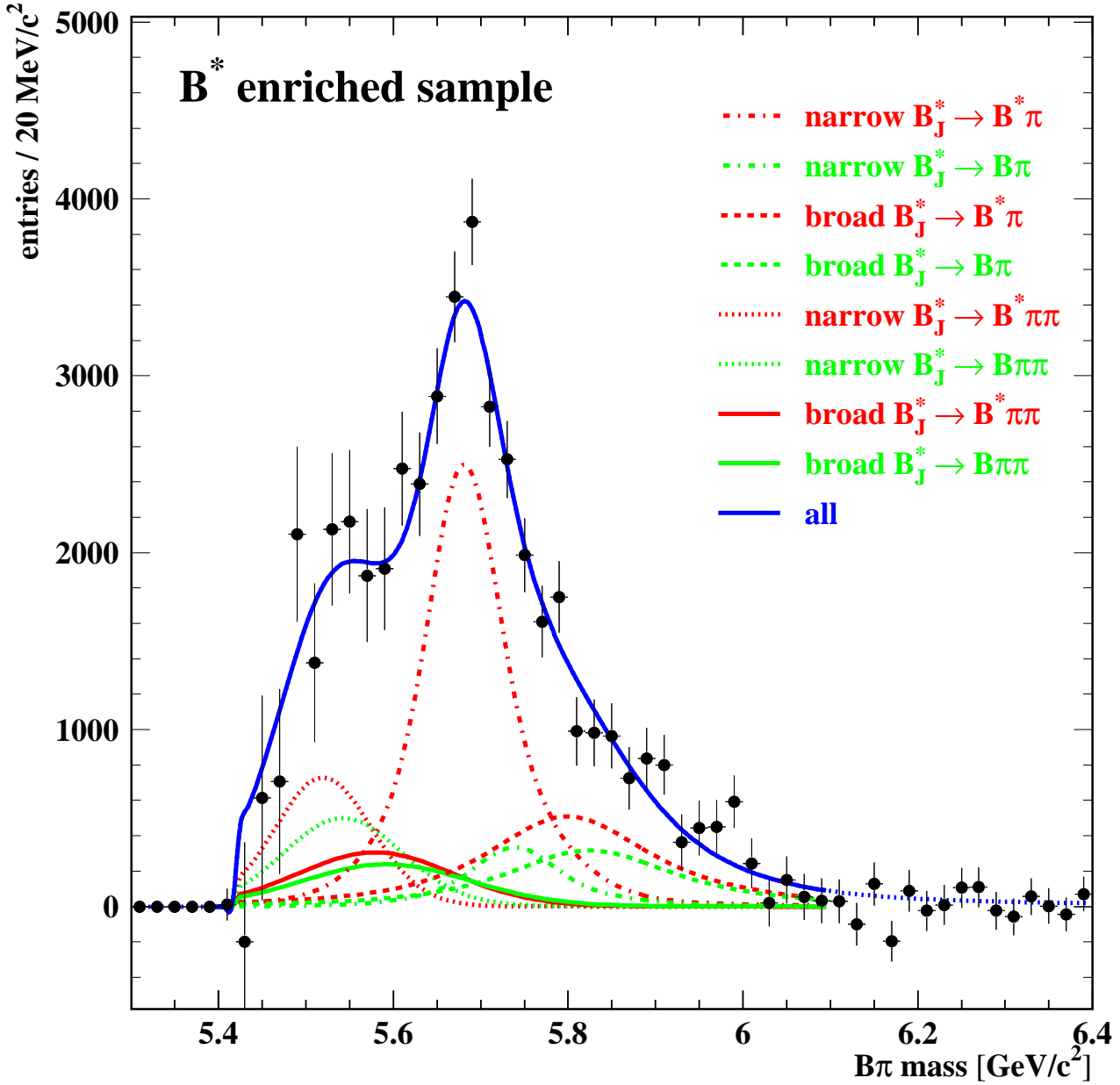
Figure 12: Simultaneous fit to the Bπ mass distributions of the B$_J^*$ samples enriched or depleted in B$_J^* \to$ B$^*\pi^\pm(\pi)$ decays (see also Figure 13). The fit results of the decays of the broad and narrow B$_J^*$ for transitions via one and two pions are presented separately.
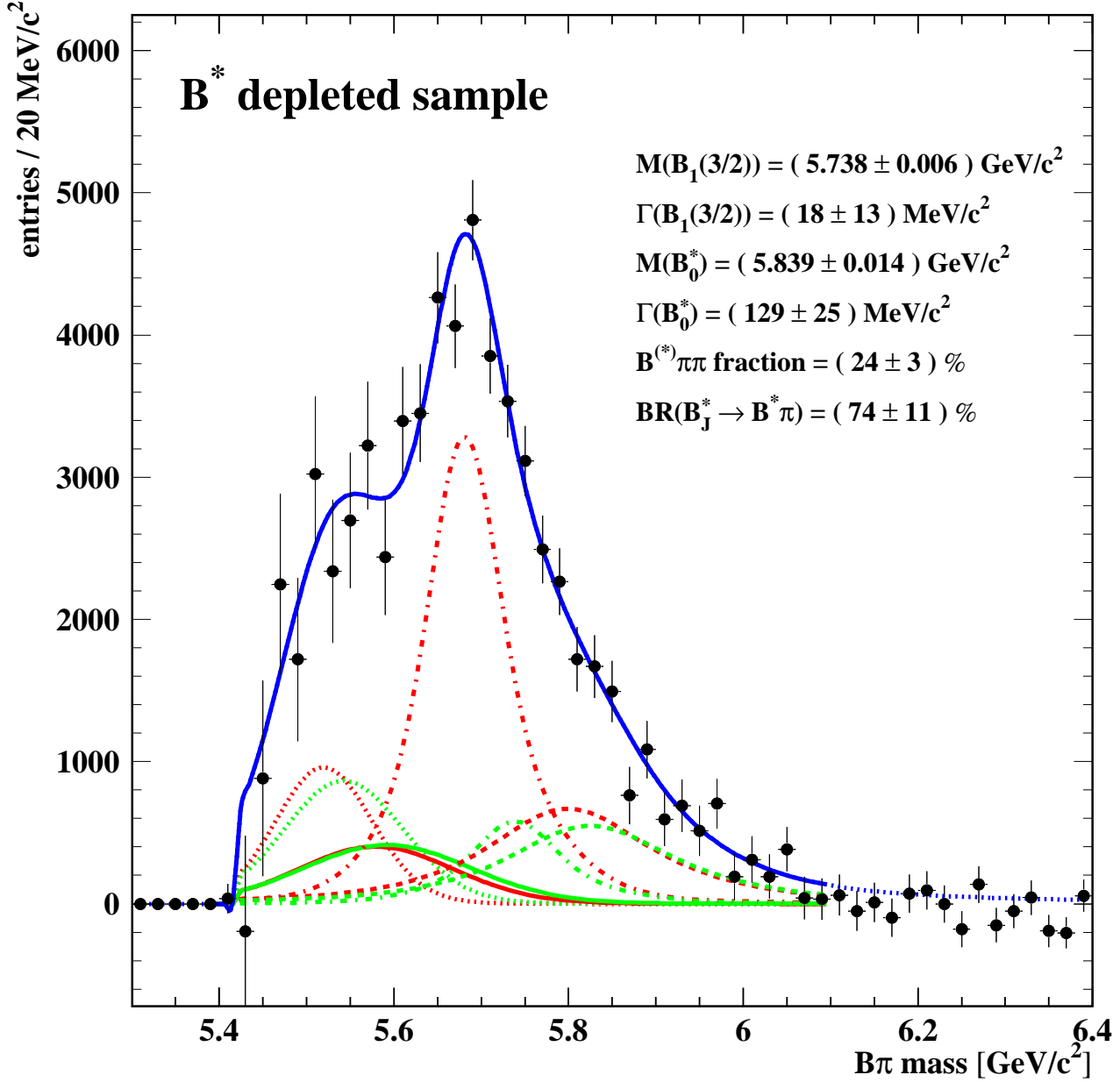
Figure 13: Simultaneous fit to the Bπ mass distribution of the B$^*_J$ samples enriched or depleted in B$^*_J \to$ B$^*\pi^\pm(\pi)$ decays. The fit results of the decays of the broad and narrow B$^*_J$ for transitions via one and two pions are presented separately. In comparison to Figure 12 the fraction of B$^*_J$ decays to B* is reduced with respect to B$^*_J$ decays to B (e.g. compare the light (B$^*_J \to$ B$^*\pi\pi$) and the dark (B$^*_J \to$ B$\pi\pi$) solid lines in Figures 12 and 13).
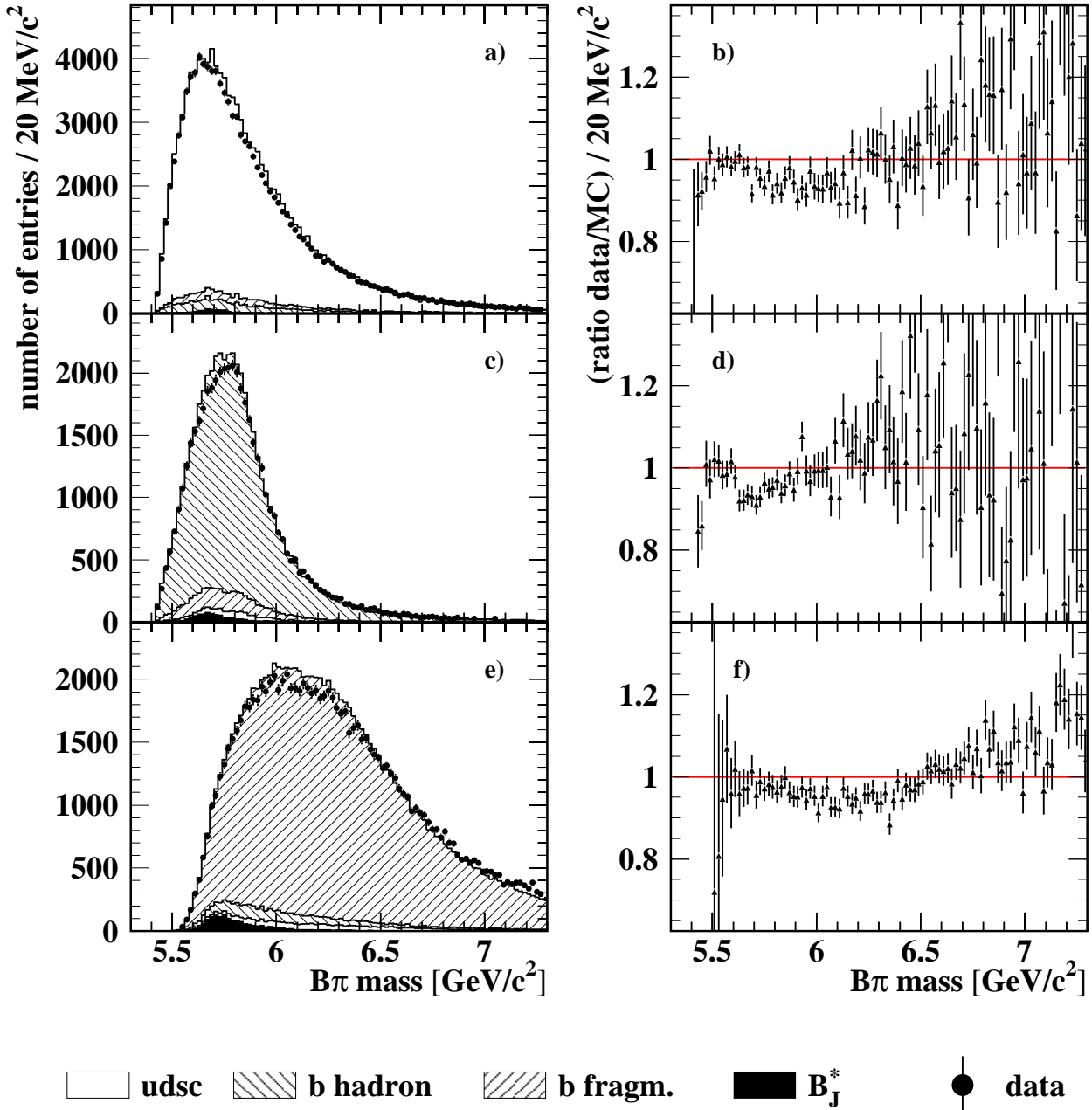
Figure 14: The B$\pi^{\pm}$ mass distributions of data and Monte Carlo for each of the three test samples (left side) and the corresponding bin-by-bin ratio of the mass distributions (right side). a)+b) Light and charm quark sample, c)+d) b hadron decay sample, e)+f) b fragmentation sample.